Journal of Power Sources 600 (2024) 234209

Contents lists available at ScienceDirect

Journal of Power Sources

journal homepage: www.elsevier.com/locate/jpowsour

Sensitivity analysis and uncertainty quantification in predictive modeling of proton-exchange membrane electrolytic cells

Violeta Karyofylli [a,*], Yannik Danner [a,b], K. Ashoke Raman [a], Hans Kungl [a], André Karl [a], Eva Jodat [a], Rüdiger-A. Eichel [a,b]

[a] Institute of Energy and Climate Research, Fundamental Electrochemistry (IEK-9), Forschungszentrum Jülich, Jülich, 52425, Germany
[b] Institute of Physical Chemistry, RWTH Aachen University, Aachen, 52062, Germany

HIGHLIGHTS

- A robust 1D computational model of PEM electrolytic cells is developed.
- The implementation is in PYTHON.
- Forward uncertainty propagation and global sensitivity analysis are carried out.
- SA highlighted the layer thicknesses' impact on the polarization behavior of PEMECs.
- The PEM thickness mostly impacts the polarization behavior at high current densities.

GRAPHICAL ABSTRACT

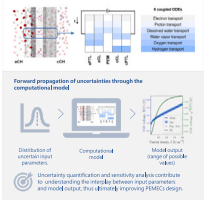

ARTICLE INFO

Keywords:
Sensitivity analysis
Uncertainty quantification
1D modeling
Nonlinear
PEM electrolytic cell
PYTHON

ABSTRACT

Insights into degradation mechanisms, lifetime prolongation, and efficiency boost-up of proton-exchange membrane (PEM) electrolytic cells (ECs) is crucial for a quick technology ramp up. Besides experiments, macro-scale modeling can contribute to the better understanding of complex mechanisms in PEM electrolytic cells (PEMECs). Modeling of PEMECs is subjective to uncertainties in operating conditions, material and design properties. Uncertainty quantification (UQ) and sensitivity analysis (SA) can highlight how uncertainties propagate from the input parameters to the output of PEMEC models. However, UQ has not found its way into PEMEC modeling yet. Thus, we apply a quasi-Monte Carlo (QMC) and polynomial chaos expansions (PCEs) framework to quantify uncertainty in a highly nonlinear PEMEC model. Specifically, we implement a fast 1D PYTHON solver, which solves a system of six nonlinear coupled ordinary differential equations (ODEs) in PEMECs. The solver robustness is an asset for the conducted UQ and global SA study since the computational model needs to be evaluated several times. The UQ and SA analysis underlines how stochastic simulations improve the prediction accuracy of PEMEC models. It also enlightens the function of PEMECs. For example, the predicted cell voltage is very sensitive to the thickness of PEM, especially when the current density increases.

1. Introduction

PEMECs have become a technology of high importance since hydrogen is an essential green energy carrier. They exhibit numerous advantages, e.g., they are environmentally friendly, operate at high current densities and offer compact balance of plant (BoP). Despite the use of rare noble materials used as catalysts, the capital expenditure (CAPEX) is thus comparatively attractive [1]. The simple PEM electrolysis (PEMEL) BoP results to a cost reduction, compared to alkaline electrolysis (AEL). Additionally, because of the high attainable current densities, a PEMEL system can be significantly smaller than an AEL system, which produces the same amount of hydrogen.

* Corresponding author.
E-mail addresses: v.karyofylli@fz-juelich.de (V. Karyofylli), ya.danner@fz-juelich.de (Y. Danner), r.kuppa@fz-juelich.de (K. Ashoke Raman), h.kungl@fz-juelich.de (H. Kungl), a.karl@fz-juelich.de (A. Karl), e.jodat@fz-juelich.de (E. Jodat), r.eichel@fz-juelich.de (R.-A. Eichel).

https://doi.org/10.1016/j.jpowsour.2024.234209
Received 28 December 2023; Received in revised form 7 February 2024; Accepted 12 February 2024
Available online 2 March 2024

Due to the high demand for commercializing PEMECs, improvements in performance and durability are mandatory. In this direction, verified and validated models can undeniably contribute to material, component, and cell optimization. However, the accuracy and predictive capabilities of mathematical and computational models have not yet been fully exploited. Reliable prognostics of PEMEC are very challenging in the field of predictive electrochemistry since PEMEC is a complex thermal, fluidic and electrochemical system [2]. Therefore, we must always consider uncertainties in experimental data, model selection, model parameters, and model inadequacy when modeling PEMECs.

Over the last decades, efforts in numerical modeling of PEMEC have been intensified [2,3]. However, these attempts have not yet reached the level of those for PEM fuel cells (PEMFCs). Most of these efforts employ commercial software. On the one hand, commercialized code provides a user-friendly environment, documentation, and support to users. On the other hand, a joint base for sharing and exchanging knowledge cannot be readily established. Fortunately, open-source code development has become more popular among scientists in the field of hydrogen research nowadays. To the authors' knowledge, only a few open-source codes capable of simulating PEMFCs/PEMEC have been implemented during recent years compared to the number of papers published on the topic and can be summarized as follows:

- OpenFCST, developed by Secanell et al. [4], a C++ package based on the DEAL.II finite element library.
- OPEM, developed by Haghighi et al. [5], is the open-source PEMFCs simulation tool for evaluating the performance of PEMFCs and is written in PYTHON. This package includes both static and dynamic models. It also comes with a graphical user interface (GUI), called GOPEM.
- OpenPNM, developed by Gostick et al. [6], is used to study porous media of PEMFCs. It is based on a pore-network model implementation in PYTHON/SCIPY.
- FAST-FC, developed by Harvey [7], is an open-source modeling toolbox for PEMFCs and other types of fuel cells and electrolyzers. It is based on FOAM-Extend, which is a fork of the open source field operation and manipulation (OpenFOAM) C++ library.
- pemfcSinglePhaseModel, developed by Kone et al. [8], is an open-source code toolbox capable of predicting the distribution of different physical quantities within PEMFCs. It has been also created using OpenFOAM, which is a C++ library.
- MMM1D, developed by Vetter and Schumacher [9], implements the most essential through-plane transport processes in a five-layer membrane-electrode assembly (MEA) (1D). In addition, it is implemented as a standalone matrix laboratory (MATLAB) function, based on MATLAB's standard boundary value problem solver. MATLAB is mainly written in C.
- PEMWE_1DModel, developed by García-Salaberri [10], is an 1D multi-phase, non-isothermal model of a PEMEC. It is based on the standalone MATLAB function of Vetter and Schumacher [9].
- p2d_pemfc_2phase, developed by Randall [11], sets out to identify limiting transport phenomena within PEMFCs fabricated with low platinum (Pt) loadings. This model uses a finite volume method for the spatial discretization and is written in PYTHON.
- fuelcellFoam, developed by Weber et al. [12], is a three-dimensional, steady-state, non-isothermal PEM fuel cell model. It is implemented in the open-source finite volume library OpenFOAM.
- openFuelCell2, developed by Zhang et al. [13], is a toolbox for simulating electrochemical devices such as fuel cells and electrolysis. The solver is based on the open-source library OpenFOAM.

To summarize the above list, most open-source software is implemented for PEMFCs instead of PEMECs. The PEMEC_1DModel, developed by García-Salaberri [10], belongs to a few exceptions. Even though this code is public, its dependency on MATLAB introduces some limitations to the users since MATLAB itself is a propriety commercial software. Concerning predictive modeling for PEMECs, García-Salaberri [10] performed a parametric analysis by changing one parameter at a time (OAT) and observed its effect on the model output. This analysis is the most straightforward and most commonly used, but it does not consider the fact that input parameters can simultaneously vary. There are other more elaborate techniques, such as the local and global SA, which can highlight in more detail the impact of every input parameter on the model output and quantities of interest (QoIs). Local and global SA has been extensively applied to modeling of PEMFCs, but not of PEMECs, unfortunately.

In a two-part paper series for PEMFCs [14,15], a macro-homogeneous two-phase MEA model, developed by Vetter and Schumacher [9] was run with a comprehensive set of material parameterizations taken from the literature. Their ultimate goal was to determine the most critical transport parameters in the model, ensuring predictions of sufficient confidence level. A prerequisite is the accurate experimental characterization of these transport coefficients, which is unfortunately not always possible. In the second part [15], they employed the two-phase model developed in the first part [9,14] for extensive forward uncertainty propagation analyses. They conducted a local parameter sensitivity study near the base-case parameter set and a global sensitivity analysis, covering a broad range of operating conditions and material properties.

Furthermore, Goshtasbi et al. [16] developed a framework for effective parametrization of PEMFCs and presented a systematic procedure for identifiability analysis. They also analyzed the sensitivity of a PEMFC-model output to numerous structural and fitting parameters. Their study was local. A global analysis based on Monte Carlo (MC) methods would have been ideal to investigate the parameter interaction. However, they stated that such analysis often becomes computationally infeasible for large-scale models. Similarly, Pant et al. [17] used a comprehensive 2D MEA model, performed a local sensitivity analysis and identified the model parameters that impact the model predictions most.

Opposed to the works on local sensitivity analysis mentioned above, a global sensitivity technique was presented by Laoun et al. [18], which was applied to a model for the simulation of the power output of PEMFCs. They investigated in depth which input parameters primarily influenced the model output. However, the 0D model used in this paper was of low fidelity. Similarly, Xu et al. [19] constructed a complete control-oriented 0D model and examined the uncertainties of model parameters and internal states based on MC simulation. They stated that malfunctions and degradation of PEMFCs can be caused by uncontrolled operating conditions/parameters since the system is susceptible to them. Recently, Liu et al. [20] proposed a method to estimate the parameters of a semi-empirical output-voltage model based on variational Bayes (VB). Utilizing Sobol sensitivity analysis, they investigated the relationship between the to-be-identified model parameters and the output voltage computed under noise and different operating conditions. They indicated how essential an accurate model for PEMFCs is for its characterization, performance analysis, and design of optimal control strategies. They also touched on the high stochasticity and parameter uncertainty of PEMFCs due to various disturbances and measurement noise while operating.

Zhou et al. [21] proposed a 2D real-time modeling approach for PEMFCs, which covers multi-physical domains for both fluidic and electrochemical features. They also performed global parameter sensitivity analysis based on Sobol indices (SI) [22]. They pointed out its importance for degradation understanding, parameter tuning and recalibration, and online prognostic. Following the same philosophy, Kannan et al. [23] claimed that developing robust control strategies is indispensable for efficiency enhancement, performance maintenance, and lifetime prolongation of PEMFCs operating under diverse conditions. They also pointed out the dependence of control-strategy reliability on the uncertainties in extrinsic and intrinsic input parameters. Therefore, they performed a MC simulation to correlate the simultaneous variation

Table 1
Governing equations for the model at hand.

Name	Unknown variable	Flux	Continuity equation	
Ohm's law for electrons	ϕ_e	$j_e = -\sigma_e^{\text{eff}} \nabla \phi_e$	$\nabla \cdot j_e = S_e$	(2)
Ohm's law for protons	ϕ_p	$j_p = -\sigma_p^{\text{eff}} \nabla \phi_p$	$\nabla \cdot j_p = S_p$	(3)
Water transport in ionomer	λ	$j_\lambda = -\frac{D_\lambda}{V_m} \nabla \lambda + \frac{\xi}{F} j_p$	$\nabla \cdot j_\lambda = S_\lambda$	(4)
Fick's law for water vapor	x_{H_2O}	$j_{H_2O} = -CD_{H_2O} \nabla x_{H_2O}$	$\nabla \cdot j_{H_2O} = S_{H_2O}$	(5)
Fick's law for oxygen	x_{O_2}	$j_{O_2} = -CD_{O_2} \nabla x_{O_2}$	$\nabla \cdot j_{O_2} = S_{O_2}$	(6)
Fick's law for hydrogen	x_{H_2}	$j_{H_2} = -CD_{H_2} \nabla x_{H_2}$	$\nabla \cdot j_{H_2} = S_{H_2}$	(7)

Table 2
Source terms.

Source	aPTL	aCL	PEM	cCL	cPTL
S_e	0	$-R_a$	–	R_c	0
S_p	–	R_a	0	$-R_c$	–
S_λ	–	$S_{ad} - S_F$	0	S_{ad}	–
S_{H_2O}	0	$-S_{ad}$	–	$-S_{ad}$	0
S_{O_2}	0	$S_F/2$	–	–	–
S_{H_2}	–	–	–	S_F	0

of the input parameters to the cell performance and to rank the critical parameters using sensitivity analysis. Pan et al. [24] also stated that the performance of PEMFCs depends on various parameters, and sensitivity analysis contributes to the optimization of the fuel cell performance. Therefore, they used a 3D non-isothermal model and performed a multi-parameter sensitivity analysis using the MC method.

All the above references have highlighted the importance of SA and UQ for the efficiency improvement and lifetime prolongation of PEMFCs. To the authors' knowledge, no such studies have been performed for PEMECs. Thus, this work aims to propagate uncertainties of the input parameters into the model output and estimate its sensitivity to them based on PCEs. A prerequisite for this propagation is first to develop an efficient and robust computational model for PEMECs. The model includes the five layers, i.e., the anodic porous transport layer (aPTL), the anodic catalyst layer (aCL), the membrane (MEM), the cathodic catalyst layer (cCL) and the cathodic porous transport layer (cPTL) between the anodic channel (aCH) and cathodic channel (cCH). These channels are not considered in the current implementation. The electrochemistry model comprises the charge balance equations for electrons and protons, the transport of water in ionomer, and the continuity equations for all gas species in our system, which are three in total (e.g., hydrogen, oxygen, and water vapor). Moreover, the reactions respect Butler–Volmer kinetics in the main application of this work.

The high-aspect-ratio PEMEC lends itself to a 1D analysis, meaning the electrochemistry model consists of a set of 1D steady ODEs. This 1D model is very cost-efficient and enables later development towards "real-time" simulations. It is also a prerequisite for our UQ and global SA purposes, which require numerous model evaluations for sampling the uncertainty space. Specifically, we have conducted an initial sensitivity-analysis study using the libraries Chaospy [25] and Uncertainpy [26] in combination with the PEMEC solver to determine which input parameters (i.e., conductivity coefficients and transport parameters) mainly influence the quantities of interest, e.g., the cell voltage.

In the following sections of this publication, the mathematical model with the governing equations and the corresponding computational models are presented, followed by a discussion on SA and UQ. Additionally, we validate our computational results against experimental data and perform SA. We finalize this work with a summary, some concluding remarks, and future plans.

2. Mathematical model

An electrolyzer is an electrochemical energy conversion device that directly converts electrical energy to chemical energy. In PEMECs, water is supplied to the device, which reaches the aCL through the aPTL. At the aCL, an oxygen evolution reaction (OER) takes place:

$$H_2O \rightarrow \frac{1}{2}O_2 + 2H^+ + 2e^-,$$

which is responsible for the dissociation of water into oxygen, protons, and electrons. Electrons create an electric current by flowing through an external circuit, while protons cross the PEM. Finally, in the cCL, a hydrogen evolution reaction (HER) takes place:

$$2H^+ + 2e^- \rightarrow H_2,$$

where electrons and protons get combined and create gaseous hydrogen. The net reaction in PEMECs can be summarized as:

$$H_2O \rightarrow \frac{1}{2}O_2 + H_2,$$

In the sections below, we describe thoroughly the one-dimensional continuum model, further investigated in this work, including its assumptions, equations, boundary conditions, and parameters. This description is necessary for the reproducibility of our results by the readers. The mathematical model is based on the work of Trinke [27] and García-Salaberri [10]. Similar models have been derived for PEMFCs by Vetter and Schumacher [9],Goshtasbi et al. [28] and Sulzer et al. [29]. This 1D model serves the purposes of SA and forward propagation of uncertainties very well. Its computational implementation in Python is very robust and fast, which makes it ideal for uncertainty quantification with QMC and PCEs.

2.1. Governing equations

The 1D model focuses on the electrochemical processes and transport phenomena occurring in the porous transport layers (PTLs), catalyst layers (CLs), and the PEM, which separates the system into the anode and cathode sides. The computation domain Ω consists of the five layer within PEMECs, and each layer denotes a different interval Ω_i with $i \in [0, 4]$. Furthermore, there are four interfaces between the domain intervals, denoted as I_j with $j \in [0, 5]$. Here, I_0 and I_5 stand for the outer boundaries. The supplementary Fig. A.1 shows a schematic overview of computation domain Ω.

All the transport phenomena are assumed to be stationary and isothermal. As described earlier, it is assumed that gas species are produced due to OER and HER (oxygen, hydrogen), behave as ideal gases, and do not cross over PEM. In addition, the reactions respect Butler–Volmer kinetics. Regarding the material components of MEA, they are supposed to be macroscopically homogeneous.

The 1D five-layer MEA model can be described by six in total ODEs, as summarized in Table 1. These ODEs are Poisson-like equations and can be generalized as:

$$\nabla \cdot \left(\mathbf{F}\left(\mathbf{u}(x), \frac{\partial \mathbf{u}(x)}{\partial x} \right) \right) = \mathbf{S}(\mathbf{u}(x)), \tag{1}$$

where the term $\mathbf{F}\left(\mathbf{u}(x), \frac{\partial \mathbf{u}(x)}{\partial x}\right)$ represents a vector of fluxes (c.f. third column of Table 1). These fluxes depend on the vector of unknown variables, $\mathbf{u}(x)$ (c.f. second column of Table 1), containing the electronic and protonic potential, ϕ_e and ϕ_p, respectively, the water-content, λ, and the molar fraction of the kth gas species, x_k. In this model, we account for three gas species, namely oxygen, hydrogen and water vapor. In the right-hand side of Eq. (1), $\mathbf{S}(\mathbf{u}(x))$ is a vector of source terms. All the right-hand-side terms are defined in Table 2.

From the supporting Fig. A.1, it is evident that different transport mechanisms dominate in disparate components of the domain. On top of that, discontinuities are also evident. Therefore, adequate boundary

Table 3
Boundary conditions.

Variable	aCH/aPTL	aPTL/aCL	aCL/PEM	PEM/cCL	cCL/cPTL	cPTL/cCH
ϕ_e	Potentiostatic mode: $\phi_e = U$ Galvanostatic mode: $-\sigma_e^{\text{eff}} \nabla \phi_e = I$	continuity	$n \cdot j_e = 0$	$n \cdot j_e = 0$	continuity	$\phi_e = 0$
ϕ_p	–	$n \cdot j_p = 0$	continuity	continuity	$n \cdot j_p = 0$	–
λ	–	$n \cdot j_\lambda = 0$	continuity	continuity	$n \cdot j_\lambda = 0$	–
x_{H_2O}	$x_{H_2O} = x_{H_2O,a}$	continuity	$n \cdot j_{H_2O} = 0$	$n \cdot j_{H_2O} = 0$	continuity	$x_{H_2O} = x_{H_2O,c}$
x_{O_2}	$x_{O_2} = x_{O_2,a}$	continuity	$n \cdot j_{O_2} = 0$	–	–	–
x_{H_2}	–	–	–	$n \cdot j_{H_2} = 0$	continuity	$x_{H_2} = x_{H_2,c}$

Table 4
Operating conditions and constants for baseline case.

Parameter	Symbol	Unit	Value	Reference
Reference temperature	T^{ref}	K	353.15	–
Operating temperature	T	K	353	–
Reference pressure	P_g^{ref}	N m^{-2}	$1.0135 \cdot 10^5$	–
Operating pressure	$P_{g,a/c}$	N m^{-2}	$1 \cdot 10^5$	–
Relative humidity	RH	–	0.90	[9]
Water saturation	s	–	0.5	–

conditions (BCs) must be defined for every neighboring component and all ODEs. These BCs are listed in Table 3. As mentioned above, the membrane is considered to be impermeable to all gas species and water vapor. Furthermore, the PEM is not electron conductive. Therefore, the normal fluxes of gas species, water vapor, and electrons are equal to zero on the interface between the PEM and catalyst layers. Protons and dissolved water content are only transported in CLs and PEM. Thus, zero-flux BCs are applied to the interfaces between CLs and the PTLs. Regarding the electrostatic potential, it is set to zero at the outer boundary of cPTL, whereas either constant voltage or current can be applied on the aPTL boundary, as illustrated in Table 3. On the rest of the inner interfaces, continuity is assumed.

In the later sections, we will give a more detailed overview of all the transport mechanisms in PEMECs. The required input parameters and the operating conditions are also explained thoroughly, but they are also summarized in Tables 4–6.

2.1.1. Electronic charge (aPTL , aCL, cCL, cPTL) and protonic charge (aCL, PEM, cCL)

Eqs. (2) and (3) describe the potential distribution and have already been given in Table 1 (first two rows). The same holds for the source terms and boundary conditions (Tables 2 and 3, respectively). In the catalyst layers, the OER and HER occur, resulting in the production and consumption of protons and electrons, respectively. As supporting information, we provide the supplementary Fig. A.2, where the local potential distribution of electron (ϕ_e) and proton (ϕ_p) is presented. The boundary conditions are also included in this schematic overview.

Here, let us focus on some terms and input parameters in Eqs. (2) and (3). For example, the effective electron conductivity is noted by σ_e^{eff} and varies between the different components in PEMECs but remains constant in each of them (please see Table 6). The effective proton conductivity, σ_p^{eff}, locally varies within CLs and PEM since it depends on the water content, λ. Its local variation will be further commented in Section 5.1. It is also a function of the ionomer volume fraction, ε_m, and temperature, T, as shown below:

$$\sigma_p^{\text{eff}} = \varepsilon_m^{1.5} 110 (f_v - 0.06)^{1.5} \exp\left[\frac{E_\sigma}{R}\left(\frac{1}{T^{\text{ref}}} - \frac{1}{T}\right)\right], \tag{8}$$

where f_v is the water volume fraction in the ionomer phase and is denoted as:

$$f_v = \frac{\lambda V_w}{\lambda V_w + V_m}. \tag{9}$$

with $V_{m/w}$ being the molar volume of dry electrolyte per SO_3^- group or the molar volume of liquid water and equal to $\frac{EW_{m/w}}{\rho_{m/w}}$. The term $EW_{m/w}$ is the equivalent weight of the dry membrane (membrane mass per SO_3^- group) or water, and $\rho_{m/w}$ is the density of electrolyte or water. In Eq. (8), E_σ stands for the activation energy, R is the ideal gas constant, and T^{ref} is a reference temperature.

Reaction rates $R_{a/c}$: As mentioned earlier, the corresponding reaction rates are described by Butler–Volmer kinetics, and further information about them can be found in the work of García-Salaberri [10], Trinke [27]:

$$R_{a/c} = i_{0,a/c} a_{a/c}^{\text{cat}} \left[\exp\left(\frac{2a_{a/c}F}{RT}\eta_{a/c}\right) - \exp\left(-\frac{2\left(1-a_{a/c}\right)F}{RT}\eta_{a/c}\right)\right]. \tag{10}$$

In Eq. (10), F is Faraday's constant, $a_{a/c}$ is the charge transfer coefficient of the half-reactions, $a_{a/c}^{\text{cat}}$ is the CLs-specific surface area, $\eta_{a/c}$ is the activation overpotential, and $i_{0,a/c}$ is the exchange current density. The subscript, a/c, in all the symbols above stands for anodic or cathodic. The exchange current density $i_{0,a/c}$ is calculated by the Arrhenius temperature correction [30,31]:

$$i_{0,a/c} = i_{0,a/c}^{\text{ref}} \exp\left[\frac{E_{A,a/c}}{R}\left(\frac{1}{T^{\text{ref}}} - \frac{1}{T}\right)\right], \tag{11}$$

where $i_{0,a/c}^{\text{ref}}$ is the reference exchange current density and $E_{A,a/c}$ is the activation energy of the respective evolution reaction. Trinke [27] has simplified this approach for the isothermal case to:

$$i_{0,a/c} = i_{0,a/c}^{\text{ref}} \exp\left(\frac{E_{\text{A},a/c}}{R\,T}\right). \tag{12}$$

Moreover, the activation overpotentials at the anode and the cathode side are respectively defined as:

$$\eta_a = \phi_e - \phi_p - E_a^{\text{rev}}, \quad \text{and} \tag{13}$$

$$\eta_c = \phi_p - \phi_e - E_c^{\text{rev}}, \tag{14}$$

where the reversible voltage of the OER or HER are denoted as $E_{a/c}^{\text{rev}}$ and computed based on the Nernst equation:

$$E_a^{\text{rev}} = \frac{\Delta H_a - T\Delta S_a}{2F} + \frac{RT}{4F}\log\left(\frac{P_{\text{O}_2}}{P_g^{\text{ref}}}\right), \quad \text{and} \tag{15}$$

$$E_c^{\text{rev}} = \frac{\Delta H_c - T\Delta S_c}{2F} + \frac{RT}{2F}\log\left(\frac{P_{\text{H}_2}}{P_g^{\text{ref}}}\right). \tag{16}$$

The value for the CLs-specific surface area varies highly in the literature [32]. García-Salaberri [10] and Chen et al. [33] consider the dependency of the specific surface area to the liquid water saturation s, as in the relation below:

$$a_{a/c}^{\text{cat}} = a_{0,a/c}^{\text{cat}} \cdot s^{n_s}, \tag{17}$$

with n_s being a coverage factor ($n_s = 0$ for the cCL and $n_s = 2$ for the aCL [10]) and $a_{0,a/c}^{\text{cat}} = 0.5 \cdot 10^7\ \text{m}^{-1}$ for both CLs in García-Salaberri

Table 5
Base-case parameters and constants.

Parameter	Symbol	Unit	Value	Reference
Faraday constant	F	$\mathrm{C\,mol^{-1}}$	96 485.33	–
Gas constant	R	$\mathrm{J\,K^{-1}\,mol^{-1}}$	8.314	–
Density of dry membrane	ρ_m	$\mathrm{kg\,m^{-3}}$	$1.97\cdot10^{3}$	[10,34]
Equivalent weight of dry membrane	EW_m	$\mathrm{kg\,mol^{-1}}$	1.02	[10,35]
Density of water	ρ_w	$\mathrm{kg\,m^{-3}}$	$0.997\cdot10^{3}$	[10]
Equivalent weight of water	EW_w	$\mathrm{kg\,mol^{-1}}$	$18\cdot10^{-3}$	[10]
Activation energy of proton conduction	E_σ	$\mathrm{J\,mol^{-1}}$	$8\cdot10^{3}$	[9,10]
Diffusion activation energy	E_λ	$\mathrm{J\,mol^{-1}}$	$2\cdot10^{4}$	[9,10]
Sorption/Desorption activation energy	$E_{a/d}$	$\mathrm{J\,mol^{-1}}$	$2\cdot10^{4}$	[9,10]
Ref. sorption coefficient	k_a^{ref}	$\mathrm{m\,s^{-1}}$	$3.53\cdot10^{-4}$	[9,10]
Ref. desorption coefficient	k_d^{ref}	$\mathrm{m\,s^{-1}}$	$1.42\cdot10^{-3}$	[9,10]

Table 6
Structural, reaction-kinetic, and transport properties.

Parameter	Symbol	Unit	aPTL	aCL	PEM	cCL	cPTL	Reference
Material	–	–	Ti	IrO_2	Nafion	Pt/C	Carbon	–
Cat. particle diameter	$d_{a/c}^{\mathrm{cat}}$	nm	–	8	–	5	–	[27,36,37]
Cat. volume fraction	$\epsilon_{a/c}^{\mathrm{cat}}$	–	–	0.45	0	0.45	–	[27,38]
Ionomer volume fraction	ϵ_m	–	–	0.3	1	0.3	–	[10,35,39]
Pore volume fraction	ϵ_p	–	0.4	0.4	–	0.4	0.4	[9,35]
Pore tortuosity	τ_p	–	1.6	1.6	–	1.6	1.6	[9]
Layer thickness	l_{Ω_i}	mm	20	$12\cdot10^{-3}$	$180\cdot10^{-3}$	$12\cdot10^{-3}$	20	[10]
Ref. exchange current density	$i_{0,a/c}^{\mathrm{ref}}$	$\mathrm{A\,m^{-2}}$	–	10^{-3}	–	10	–	
Activation energy	$E_{A,a/c}$	$\mathrm{J\,mol^{-1}}$	–	$4\cdot10^{4}$	–	$2\cdot10^{4}$	–	[10]
Charge transfer coefficient	$a_{a/c}$	–	–	0.5	–	0.5	–	[31,40]
Cat. layer specific surface area	$a_{a/c}^{\mathrm{cat}}$	$\mathrm{m^{-1}}$	–	$2\cdot10^{7}$	–	$2\cdot10^{7}$	–	
Eff. electric conductivity	σ_e^{eff}	$\mathrm{S\,m^{-1}}$	1250	350	–	350	1250	[9,10,39,41]
Enthalpy change of OER/HER	$\Delta H_{a/c}$	$\mathrm{J\,mol^{-1}}$	–	$285.83\cdot10^{3}$	–	0	–	[9,10,42]
Entropy change of OER/HER	$\Delta S_{a/c}$	$\mathrm{J\,mol^{-1}\,K^{-1}}$	–	163.3	–	−0.104	–	[9,10,42]
Ref. diffusivity of water vapor	$D_{H_2O,a/c}^{\mathrm{ref}}$	$\mathrm{m^2\,s^{-1}}$	$0.36\cdot10^{-4}$	$0.36\cdot10^{-4}$	–	$1.24\cdot10^{-4}$	$1.24\cdot10^{-4}$	[9,10,40,43]

[10]. Trinke [27] calculates the specific surface area from the catalyst layer's properties as follows:

$$a_{a/c}^{\mathrm{cat}} = 6\frac{\epsilon_{a/c}^{\mathrm{cat}}}{d_{a/c}^{\mathrm{cat}}}. \tag{18}$$

In Eq. (18), $\epsilon_{a/c}^{\mathrm{cat}}$ is the catalyst fraction, and $d_{a/c}^{\mathrm{cat}}$ is the catalyst particle diameter. This leads to $a_a^{\mathrm{cat}} = 33.57\cdot10^{7}$ and $a_c^{\mathrm{cat}} = 54\cdot10^{7}\ \mathrm{m^{-1}}$. Thereby, the variability in calculations of CLs-specific surface area is an uncertainty factor in predictive modeling and will be discussed further in Section 5.1.

2.1.2 Water transport in ionomer (aCL , PEM, cCL)

Another critical process in the system is the transport of dissolved water in the ionomer phase, referred to as water content, λ. It expresses the humidification level and equals the water molecules per acidic group. The water content diffuses within the ionomer phase of the membrane and catalysts due to moisture gradient and the electro-osmotic drag, as explained by Trinke [27]. The equation describing this transport mechanism is Eq. in Table 1. In this equation, the water diffusivity in the ionomer phase is denoted as D_λ, and is equal to:

$$D_\lambda = \epsilon_m^{1.5}\frac{3.842\lambda^3 - 32.03\lambda^2 + 67.74\lambda}{\lambda^3 - 2.115\lambda^2 - 33.013\lambda + 103.37}10^{-10}\exp\left[\frac{E_\lambda}{R}\left(\frac{1}{T^{\mathrm{ref}}} - \frac{1}{T}\right)\right], \tag{19}$$

where E_λ is the activation energy of water-content diffusion. Eq. (19) is provided by Vetter and Schumacher [9], who refitted a λ-dependent polynomial to experimental data for Nafion membranes of Mittelsteadt and Staser [44].

Further description should be given for electro-osmotic drag (EOD) term $\frac{\xi}{F}j_p\nabla\cdot j_\lambda$ and the source term, S_λ, in . Here, S_λ includes the sorption/desorption of liquid/dissolved water in the ionomer of both catalysts layers (S_{ad}) and the electrochemical consumption of water content in the anode catalyst layer (S_F).

EOD term $\frac{\xi}{F}j_p\nabla\cdot j_\lambda$: In , the symbol, ξ, stands for the EOD coefficient and is a linear function of λ:

$$\xi = \frac{2.5\lambda}{22} \tag{20}$$

Berning [45] has conducted a thorough review of EOD and its coefficient, which indicates the number of water molecules transported by each proton. Eq. (20) has been formulated by Springer et al. [46] and was calculated out of two measurement points ($\lambda = 11,\ \xi = 0.9$) and ($\lambda = 22,\ \xi = 2.5$) [47]. The work of Zawodzinski et al. [47], which was done at the same working group as Springer et al. [46], corrected the expression shown in Eq. (20) to:

$$\xi = 1, \quad 1.4 < \lambda < 14. \tag{21}$$

A similar expression was measured by Fuller and Newman [48] with:

$$\xi = 1.4, \quad 2 < \lambda < 14. \tag{22}$$

Eq. (20) is a highly recommended expression for ξ and is used in the model of Vetter and Schumacher [9] and García-Salaberri [10]. However, in the models of Zhang [49] and Chen et al. [33], the approach of Zawodzinski et al. [47] is adapted based on the second measurement point of Springer et al. [46] to the following expression:

$$\xi = \begin{cases} 1, & \lambda \le 14 \quad \text{or} \\ 1 + \frac{1.5}{8}(\lambda - 14), & \lambda > 14 \end{cases} \tag{23}$$

Later, in Section 5.1, we further investigate the effect of these different definitions of EOD coefficients on the polarization behavior of PEMECs.

Water sorption/desorption S_{ad}: The source term related to water sorption/desorption is specified below:

$$S_{ad} = \begin{cases} \frac{k_a}{l_{cl}V_m}(\lambda_{eq} - \lambda), & \lambda \le \lambda_{eq} \quad \text{(sorption)} \quad \text{or} \\ \frac{k_d}{l_{cl}V_m}(\lambda_{eq} - \lambda), & \lambda \ge \lambda_{eq} \quad \text{(desorption)}, \end{cases} \tag{24}$$

where l_{CL} is the CLs thickness. Here, the symbol $k_{a/d}$ is the sorption/desorption mass-transfer coefficient, which depends on the volume fraction of water and temperature as:

$$k_{a/d} = k_{a/d}^{\text{ref}} f_v \exp\left[\frac{E_{a/d}}{R}\left(\frac{1}{T^{\text{ref}}} - \frac{1}{T}\right)\right], \tag{25}$$

with $k_{a/d}^{\text{ref}}$ being the reference mass-transfer coefficient of sorption/desorption.

In Eq. (24), λ_{eq} describes the equilibrium water content in ionomer and is a function of relative humidity, RH, temperature, T, and saturation, s:

$$\lambda_{eq} = \left(0.05 + 20.45\text{RH} - 42.8\text{RH}^2 + 36\text{RH}^3\right)\left[1 + 0.2\text{RH}^2\left(\frac{T - 303.1}{30}\right)\right] + 6.5s. \tag{26}$$

In this work, we assume that RH and s are constant. However, we should introduce the dependency of RH on the mole fraction of water vapor $x_{\text{H}_2\text{O}}$, the gas pressure, $P_{g,a/c}$, and the saturation pressure of water vapor, $P_{H_2O}^{\text{sat}}$ in future work. It can be easily computed as:

$$\text{RH} = x_{\text{H}_2\text{O}} \frac{P_{g,a/c}}{P_{\text{H}_2\text{O}}^{\text{sat}}}, \tag{27}$$

where $P_{g,a/c}$ is the gas pressure. According to Vetter and Schumacher [9], $P_{H_2O}^{\text{sat}}$ can be estimated through Antoine equation, as follows:

$$\ln\left[\frac{P_{\text{H}_2\text{O}}^{\text{sat}}}{1\,\text{Pa}}\right] = 23.1963 - \frac{3816.44\,\text{K}}{T - 46.13\,\text{K}}. \tag{28}$$

Lastly, assuming that liquid saturation remains constant in our model is an oversimplification. For now, it does not harm our predictions concerning the polarization behavior of a PEMEC. In later work, we will enhance our implementation with an appropriate model for liquid water and gas saturation, as proposed by Zinser et al. [50], and investigate further drying-out effects.

Water consumption S_F: The consumption of water by the OER can be calculated by Faraday's law:

$$S_F = \frac{R_a}{z_{\text{H}_2\text{O}} F} \tag{29}$$

Finally, the water content in the ionomer phase is highly influential for the polarization behavior of PEMECs, as we see in Section 5.1. Other properties, such the effective protonic conductivity in Eq. (8), depend on it. A careful selection of model, describing all its transport mechanism, is a prerequisite for precise predictions.

2.1.3 Transport of gas species (aPTL , aCL, cCL, cPTL)

In this study, the main transport mechanism of gas species in the porous structure of the CLs and PTLs is assumed to be diffusion, as described by Fick's law, which can be an oversimplification of the complex transport phenomena in these porous structures. However, the overall focus of this paper is to propose an uncertainty quantification and global sensitivity analysis framework. Thus, this oversimplification is, for now, acceptable. Later, we should enhance further the modeling mechanism of gas-species transport via Darcy's law since it is capillary-dominated. Moreover, the gas-pressure distribution is presumed to be uniform, the gas species are assumed to follow the ideal gas law, so that the molar gas-phase concentration can be calculated by:

$$C_{g,a/c} = \frac{P_{g,a/c}}{RT}. \tag{30}$$

As already mentioned above, gas crossover is not considered in this study. Thus, a binary gas mixture of oxygen and water vapor exists at the anode side, whereas hydrogen mixed with water vapor exists at the cathode side. Moreover, effective diffusivities of each species in the CLs and PTLs are assumed to be equal, thus:

$$x_{\text{O}_2} = 1 - x_{\text{H}_2\text{O}} \xRightarrow{\text{Eq. (30)}} P_{\text{O}_2} = P_{g,a} - P_{\text{H}_2\text{O}}^{\text{sat}} \quad \text{(anode side), and} \tag{31}$$

$$x_{\text{H}_2} = 1 - x_{\text{H}_2\text{O}} \xRightarrow{\text{Eq. (30)}} P_{\text{H}_2} = P_{g,c} - P_{\text{H}_2\text{O}}^{\text{sat}} \quad \text{(cathode side).} \tag{32}$$

According to Vetter and Schumacher [9] and García-Salaberri [10], the effective diffusivity of water vapor in species i ($i = \text{O}_2$ in the anode and $i = \text{H}_2$ in the cathode), is equal to:

$$D_{\text{H}_2\text{O},i}^{\text{eff,wet}} = D_{\text{H}_2\text{O},i} \frac{\epsilon_p}{\tau_p^2} (1 - s)^3, \tag{33}$$

with $D_{\text{H}_2\text{O},i}$ being the molecular diffusivity of water vapor in the bulk space and defined as:

$$D_{\text{H}_2\text{O},\text{O}_2} = D_{\text{H}_2\text{O},a}^{\text{ref}} \left(\frac{T}{T^{\text{ref}}}\right)^{1.5} \left(\frac{P_g^{\text{ref}}}{P_{g,a}}\right), \text{ and} \tag{34}$$

$$D_{\text{H}_2\text{O},\text{H}_2} = D_{\text{H}_2\text{O},c}^{\text{ref}} \left(\frac{T}{T^{\text{ref}}}\right)^{1.5} \left(\frac{P_g^{\text{ref}}}{P_{g,c}}\right). \tag{35}$$

Finally, regarding the source terms in the species transport equations, they have already been defined in Table 2 and thoroughly described in Section 2.1.2.

3 Computational model

The mathematical model is entirely implemented in Python since it is among the most popular programming languages nowadays according to the PopularitY of Programming Language (PYPL) index PYP [51]. Python's popularity is based on the fact that it is user-friendly. It leads to the development of numerous open-source packages, which makes further exploration possible. In addition to that, plenty of open-source libraries originally written in C++ provide a Python interface these days, which makes them more accessible.

Algorithm 1: Reformulation of second-order ODEs in (1)

1 Define as symbolic expression the left-hand side of the system (1)

2 Differentiate the symbolic expression in Step 1 with sympy.diff to get the following:

$$\mathbf{a}(x)\frac{d^2\mathbf{u}}{dx^2} + \mathbf{b}(x)\frac{d\mathbf{u}}{dx} + \mathbf{c}(x)$$

3 After differentiation, reformulate the system (1) into:

$$\frac{d^2\mathbf{u}}{dx^2} = \frac{-\mathbf{b}(x)\frac{d\mathbf{u}}{dx} - \mathbf{c}(x) + \mathbf{S}(\mathbf{u}(x))}{\mathbf{a}(x)}$$

For solving the system of second-order ODEs (1), the solve_bvp solver from the submodule scipy.integrate is used. The solve_bvp solver is based on a fourth-order collocation method. Since the Jacobian of the system is not computed manually, it will be estimated by forward finite differences. Detailed information about it can be found in its online documentation.

However, this solver can only handle systems of first-order ODEs contingent on two-point boundary conditions. Therefore, we need to follow some steps before being able to solve the system. First of all, the system of second-order ODEs (1) needs to be reformulated through sympy.diff, as step-wisely explained in Algorithm 1. The method sympy.diff differentiates mathematical expressions with variables and belongs to the library SymPy, which is written in Python and is for symbolic mathematics.

Unlike bvp4c and bvp5c solvers, provided by MATLAB, the solve_bvp solver cannot explicitly handle multi-point BCs, but only two-point BCs. In Algorithm 2, we illustrate how to prepare multi-point BVPs for two-point BVP codes. This can be achieved by solving the system at each domain interval, Ω_i (please see Fig. A.1), and ensuring continuity

Algorithm 2: Preparation of multi-point boundary value problems (BVPs) for two-point BVP codes

1 Introduce unknowns, parameters, and source terms for each interval of the domain (e.g., $\mathbf{u}_i(x)$ instead of $\mathbf{u}(x)$):

$$\frac{d^2\mathbf{u}_i}{dx^2} = \frac{-\mathbf{b}_i(x)\frac{d\mathbf{u}_i}{dx} - \mathbf{c}_i(x) + \mathbf{S}_i(\mathbf{u}_i(x))}{\mathbf{a}_i(x)}$$

2 Apply continuity conditions to the interfaces between intervals:

$$\mathbf{u}_i(x_{I_j}) = \mathbf{u}_{i+1}(x_{I_j})$$
$$\left.\frac{d\mathbf{u}_i}{dx}\right|_{x_{I_j}} = \left.\frac{d\mathbf{u}_{i+1}}{dx}\right|_{x_{I_j}}$$

3 Solve all ODEs simultaneously on the same interval, by mapping each $[x_{I_j}, x_{I_{j+1}}]$ onto $[0,1]$ through a new independent variable:

$$\xi = \frac{x - x_{I_j}}{x_{I_{j+1}} - x_{I_j}} \Rightarrow \frac{d\xi}{dx} = \frac{1}{x_{I_{j+1}} - x_{I_j}}$$

4 Apply chain rule to the equation of **Step 3** in Algorithm 1:

$$\frac{d^2\mathbf{u}_i}{d\xi^2} = l_i^2 \frac{-\frac{\tilde{\mathbf{b}}_i(\xi)}{l_i}\frac{d\mathbf{u}_i}{d\xi} - \tilde{\mathbf{c}}_i(\xi) + \mathbf{S}_i(\tilde{\mathbf{u}}_i(\xi))}{\tilde{\mathbf{a}}_i(\xi)},$$

where $\tilde{\mathbf{d}}(\xi) = \mathbf{d}((x_{I_{j+1}} - x_{I_j})\xi + x_{I_j})$ and $l_i = x_{I_{j+1}} - x_{I_j}$

on the interfaces between them. Finally, the system of second-order ODEs (1) is transformed into a system of first-order ODEs, as carefully described in Algorithm 3.

Algorithm 3: Converting system of second-order ODEs to one of first-order ODEs

1 Replace $\frac{d\mathbf{u}_i}{d\xi}$ with $\mathbf{y}_i(\xi)$ in equation of **Step 4** in Algorithm 2:

$$\text{System of first-order ODEs} \longrightarrow \begin{cases} \frac{d\mathbf{u}_i}{\partial\xi} = \mathbf{y}_i(\xi) \\ \frac{d\mathbf{y}_i}{d\xi} = l_i^2 \frac{-\frac{\tilde{\mathbf{b}}_i(\xi)}{l_i}\mathbf{y}_i(\xi) - \tilde{\mathbf{c}}_i(\xi) + \mathbf{S}_i(\tilde{\mathbf{u}}_i(\xi))}{\tilde{\mathbf{a}}_i(\xi)} \end{cases}$$

4 Sensitivity analysis and uncertainty quantification

UQ and SA play a crucial role in analyzing, characterizing, and optimizing the impact of parameters and their uncertainties on the output of the PEMEC model. We present their importance for accurate predictions and the tools used to incorporate them in our simulations. Before giving more specific details about the framework, we would like to give a brief overview of predictive simulations and their sources of uncertainty. Oden et al. [52] stated the special meaning of *predictive simulation*:

> "The systematic treatment of model and data uncertainties, and their propagation through a computational model to produce predictions of quantities of interest with quantified uncertainty".

Furthermore, Oden [53] listed the following sources of uncertainty in predictive computational engineering science:

- $\mathcal{P}$ uncertainty, which is the systemic uncertainty and is related to the mathematical framework in which we perform uncertainty quantification.
- $\mathcal{Y}$ uncertainty, which incorporates uncertainty in observational data due to pollution with experimental noise.
- $\mathcal{M}$ uncertainty, which is related to the selection of the mathematical model itself. It determines how parameter sets $\mathbf{X}$ are mapped into the theoretical observation $\mathbf{Y}$ (see the supporting Fig. A.3).
- θ uncertainty, which embodies the uncertainty in parameter values or constitutive relations. Knowledge about these values and relations is gathered from the literature, previous experiments, or archival databases.
- h uncertainty, which is the uncertainty concerning the numerical discretization process leading to the computational model.

After introducing sources of uncertainty in numerical predictions, we comment that the approaches for UQ and SA can be classified into global and local methods. For more information, please check the supporting Fig. A.4. As already commented in the introduction, mainly for PEMFCs, local SA investigates how the model output depends on small perturbations around a nominal value of each parameter. Local SA is often limited to one parameter at a time, whereas global SA considers the whole parameter space.

For this work, global SA is employed. Global SA approaches can be further categorized into intrusive and non-intrusive methods. Intrusive methods can sometimes be challenging since the basic model equations must be changed. On the contrary, non-intrusive methods treat the model as a black box (see the supporting Fig. A.3) and can be combined with any model. Their significant advantage is that modification of the model equations or implementation is unnecessary.

Our UQ and SA framework is about forward propagating uncertainties and is based on the python package Uncertainpy, implemented by Tennøe et al. [26]. Uncertainpy depends on the python packages Chaospy [25], and SALib (Iwanaga et al. [54] and Herman and Usher [55]). It performs UQ and SA through QMC or PCEs.

The QMC method is preferred to the standard (MC) method when the parameter space is small enough and the parameters sufficiently smooth. The QMC method is faster than the MC method [56]. The QMC method improves upon the MC approach by employing a low-discrepancy sequence, e.g., the Hammersley sequence, for sampling the parameter space. Thus, the samples are more evenly distributed.

Another mathematical framework for efficient UQ and SA is PCEs [57]. PCEs are usually faster than the QMC method as long as the parameter space is small enough (parameters less than about 20). Thus, PCEs require fewer model evaluations than the QMC method while achieving the same accuracy. However, they exhibit two main limitations. The larger the parameter space, the worse the required model-evaluation number scales. In addition, their performance is reduced if the output depends on the input parameters in a non-smooth manner.

The overall goal behind UQ and SA is to quantify how the uncertain parameters influence the model output employing the following statistical metrics, which can be further explained in the work of Tennøe et al. [26]:

- The mean $\mathbb{E}$ (the expectation value): $\mathbb{E}[Y] = \int_{\Omega_Y} y f_Y(y) dy$
- The variance $\mathbb{V}$: $\mathbb{V}[Y] = \int_{\Omega_Y} (y - \mathbb{E}[Y])^2 f_Y(y) dy$
- The $(100 \cdot \chi)$th percentile: $\chi = \int_{-\infty}^{P_\chi} f_Y(y) dy$
- The prediction interval I_χ: $I_\chi = [P_{(\chi/2)}, P_{(1-\chi/2)}]$
- The first-order Sobol sensitivity index S_i: $S_i = \frac{\mathbb{V}[\mathbb{E}[Y|X_i]]}{\mathbb{V}[Y]}$

4.1 Benchmark case

To explore the capabilities of the UQ and SA framework, we use a 0D semi-empirical model that computes the polarization behavior of a

Table 7
Parameters for the 0D model with respect to a cell temperature of 80 °C, as reported by Schalenbach et al. [58].

Parameter	Unit	Minimum value (min)	Maximum value (max)
Separator resistance, R_{sep}	Ω cm^2	$\mathbf{0.126} - 0.013$	$\mathbf{0.126} + 0.013$
Electrode resistance, R_e	Ω cm^2	$\mathbf{0.029} - 0.01$	$\mathbf{0.029} + 0.01$
Tafel slope, α	V	$\mathbf{0.0133} - 0.000133$	$\mathbf{0.0133} + 0.000133$
Exchange current density, i_0	A cm^{-2}	$0.9 \cdot \mathbf{2.602} \cdot \mathbf{10^{-10}}$	$1.1 \cdot \mathbf{2.602} \cdot \mathbf{10^{-10}}$
Partial pressure increase factors, Y_{H_2} and Y_{O_2}	bar cm^2 A^{-1}	$\mathbf{3.0} - 1.0$	$\mathbf{3.0} + 1.0$

PEMEC and was presented by Schalenbach et al. [58]. This model is extensively used in the literature, and can be easily evaluated without employing the computation model described in Section 3, but provides an excellent basis to evaluate our UQ and SA framework. The current–voltage characteristics of PEMECs are described by:

$$U_{cell} = U_N + U_{\text{kin}} + U_{\Omega}, \tag{36}$$

where the terms U_N, U_{kin}, and U_{Ω} express the Nernst voltage, the kinetic overpotential, and the Ohmic drop due to electron and ion conduction, respectively. Their definition is summarized in the list below:

- Nernst voltage: $U_N = U_{\text{rev}} + \frac{RT}{2F} \ln\left(\frac{P_{\text{H}_2,c}\sqrt{P_{\text{O}_2,a}}}{P_0^{3/2} a_{\text{H}_2\text{O}}}\right)$,
- Kinetic overpotential: $U_{\text{kin}} = \alpha \ln\left(\frac{i}{i_0}\right)$ (Tafel equation),
- Ohmic drop due to electron and ion conduction: $U_{\Omega} = \left(R_e + R_{\text{sep}}\right) i$, and
- Reversible cell voltage: $U_{\text{rev}} = 1.229\ \text{V} - 0.000846\ \text{V K}^{-1}(T - 298.15\ \text{K})$.

In this 0D semi-empirical model, the kinetic overpotential is described by Tafel equation, which is a limiting case of the Butler–Volmer equation and only holds in the high overpotential region. For the results in Section 5, the Butler–Volmer equation was used instead. According to this model, the polarization behavior of a cell is a function of current density, i, partial pressures of hydrogen at the cathode and oxygen at the anode, $P_{\text{H}_2,c}$ and $P_{\text{O}_2,a}$, and temperature, T, and can be recapped in $U_{cell} = U(i, P_{\text{O}_2,a}, P_{\text{H}_2,c}, T)$. The partial pressures of hydrogen at the cathode and oxygen at the anode can be computed with the help of the following equation:

$$P_{\text{O}_2/\text{H}_2,a/c} = P_{g,a/c} + Y_{\text{O}_2/\text{H}_2}\ i - P_{sv}(T) \tag{37}$$

with $P_{sv}(T)$ being the saturated vapor pressure of water at 80 °C, which is equal to 0.49 bar. For further details, we encourage the readers to read the work of Schalenbach et al. [58], where the model of the voltage–current characteristics was originally presented.

From the above description, it is clear that the cell voltage depends on several other input parameters, which are encapsulated in Table 7 and can influence its prediction accuracy. The model is initially evaluated deterministically, meaning that the input parameters do not include any uncertainties, and single numerical values are assigned to them (mean value of Table 7, represented in bold). The computed polarization behavior of a PEMEC is depicted in Fig. 1(a). The polarization curve can be split into two primary regions. The kinetic overpotential dominates the region at low current densities. The second region from moderate to high current densities shows a linear behavior, which is closely related to the Ohmic losses. There can be a third region, which is not depicted in Fig. 1(a) because it is omitted from the model. It usually becomes apparent at very high current densities, where mass transport losses strongly increase.

Regarding model predictions and their accuracy, Schalenbach et al. [58] stated in his publication the following:

> "Uncertainties that affect the model predictions arise from the errors of the parameters and the assumptions or simplifications used. All parameters that were experimentally determined or that were extracted from the literature were characterized by an error".

Therefore, instead of assuming fixed model parameters as in a deterministic model, one can consider these parameters as random variables and assign a distribution of possible values to each. We then set up a stochastic analytical model with these random variables as coefficients and quantify the uncertainty in model predictions via either the QMC method or PCEs (Fig. 1(b)). The parameters range was chosen to include values of previous numerical studies (e.g., the work of Schalenbach et al. [58]). We assume that the uncertain input parameters are independent of each other and assign them a uniform distribution: $\mathbf{X}$, with $X_i \sim \mathcal{U}(\min, \max)$, where min and max were taken from Table 7.

In Fig. 1(b), we present the mean, standard deviation (SD), and 90% prediction interval (PI), whereas in Fig. 1(c), the first-order SI. The 1st-order SI quantify the share of variance in the model output, $\mathbf{Y}$, for every input parameter, X_i. As the mean (blue line) in Fig. 1(b) shows, the voltage rises linearly when the current density becomes higher than 0.5 A cm^2. From the sensitivity analysis (Fig. 1(c)), we see that the polarization behavior of the PEMEC is most sensitive to the resistances for current densities higher than 0.5 A cm^2. This finding is to be expected and well-known in the literature. Nevertheless, it serves well our purposes to validate our framework, understand better how global sensitivity analysis works, and choose which method (QMC or PCEs) is preferable for the more complex 1D mathematical model, whose results are reported in Section 5.

Following the example of Tennøe et al. [26], we compare the efficiency of the QMC method and PCEs by calculating the absolute relative error (ARE) of the UQ for this 0D semi-empirical model when varying the number of model evaluations, N_s. For the definition of ARE, please see Appendix A.1. Fig. 2 shows the error of the mean, variance, and first-order SI of the two methods. We observe the same as Tennøe et al. [26], namely that PCEs are much faster than the QMC method for the 0D analytical model with six uncertain input parameters. Therefore, a specific error is achieved with fewer model evaluations, N_s. For our later studies with the 1D model, we will use only PCEs to perform UQ and SA and further investigate how its several uncertain input parameters influence its output and, consequently, its prediction accuracy.

5 Results

In this section, we perform a UQ study and SA, but first, we validate our computational results against experimental data, taken from Chandesris et al. [43], by means of deterministic and stochastic simulations. These experimental data were also used by García-Salaberri [10] for validation. For the later computations, we use the base-case parameters and operating conditions as shown in Tables 4–6, unless we defined them differently below. These model input parameters are taken from the work of García-Salaberri [10], assumed well-tuned, and calibrated for the computational model.

However, we need to draw the reader's attention to the nontrivial procedure of calibrating the model parameters and constitutive relations. Calibration plays a particular role in physics-based models, whose independent variables and material-related input parameters are numerous. The traditional way of calibration is via manual tuning, e.g., a trial-and-error approach. Manual tuning usually requires strenuous efforts but does not provide any UQ and cannot guarantee the degree of parameter-set uniqueness, as highlighted by Nguyen et al. [59]. Thus, calibration by trial and error might lead to inaccurate

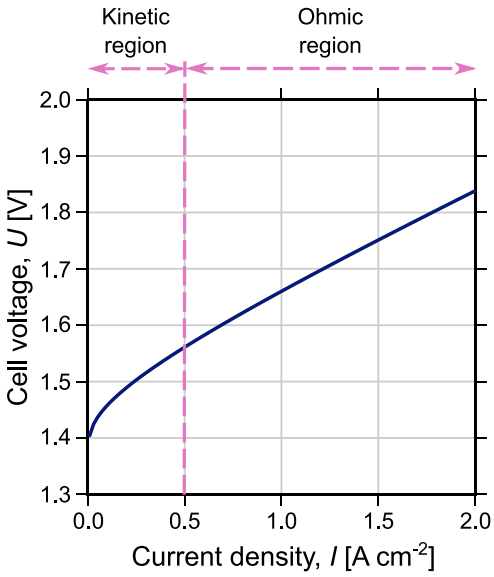

(a) Cell potential of a PEMEC based on deterministic modeling.

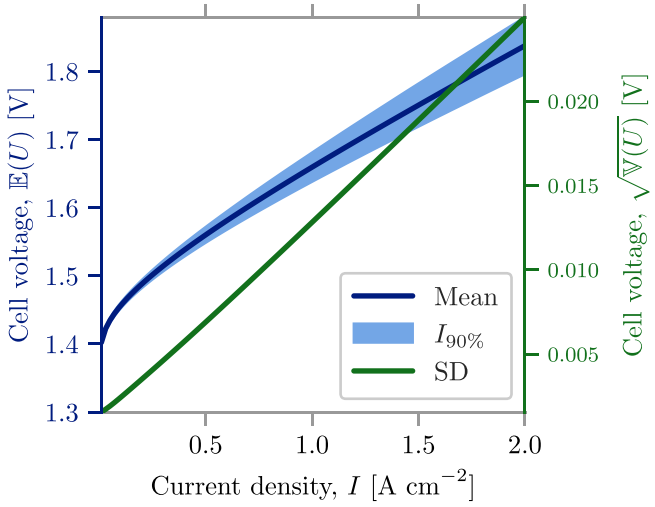

(b) Cell potential of a PEMEC based on stochastic modeling.

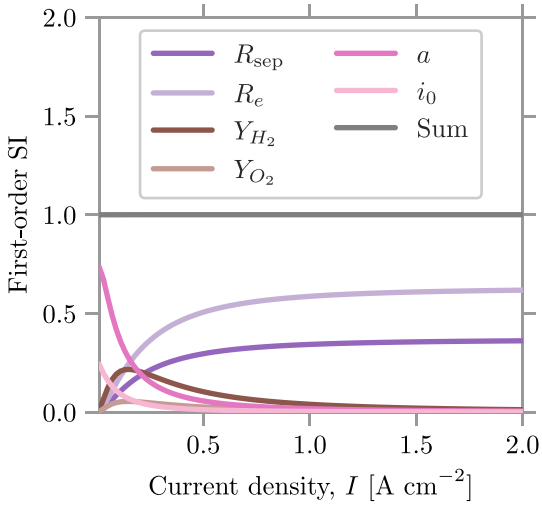

(c) First-order SI

Fig. 1. Polarization behavior at 80 °C by means of the 0D semi-empirical model (1(a) and 1(b)). SA of the polarization behavior 1(c), while using PCEs.

predictions. Other experiments than the main application of interest, which needs to be precisely simulated by physics-based models, need to be thoughtfully designed and conducted for parameter estimation and calibration.

5.1 Comments on θ uncertainty in predictive modeling for PEMEC

In Section 4, we summarized the uncertainties in predictive simulation, and here, we will take a closer look at θ uncertainty, the uncertainty concerning input parameters of physics-based models. These input parameters include material properties, transport parameters, or other constitutive relations and are usually estimated based on literature, archival databases, or experiments, as we described earlier. Unfortunately, Vetter and Schumacher [14] pointed out the following:

> "Experimental data published on several transport coefficients are scattered over orders of magnitude, even for the most extensively studied materials such as Nafion membranes, for instance".

Thus, our goal to have well-calibrated input parameters for our physics-based model is not trivial. Manual calibration is not the way to go. Instead, sophisticated methods, such as Bayesian inference, should be applied to calculate these parameters within a PI and provide the uncertainty level in their estimated values by accounting for the considerable variability of experimental observation.

In this work, we use two exemplary parameters to demonstrate how uncertainty in their values can lead to discrepancies. These input parameters can be complex to be determined from experimental studies; their values vary widely within the literature. They are the following: the electro-osmotic drag (EOD) coefficient and the product of reference exchange current density with the volume-specific surface area of the catalyst layers.

EOD coefficient In Section, we described two constitutive relations for the EOD coefficient, one provided by Springer et al. [46] (Eq. (20)) and one by Zawodzinski et al. [47] as adapted by Zhang [49] (Eq. (23)). The second one was actually the correction outcome of misfitted models on

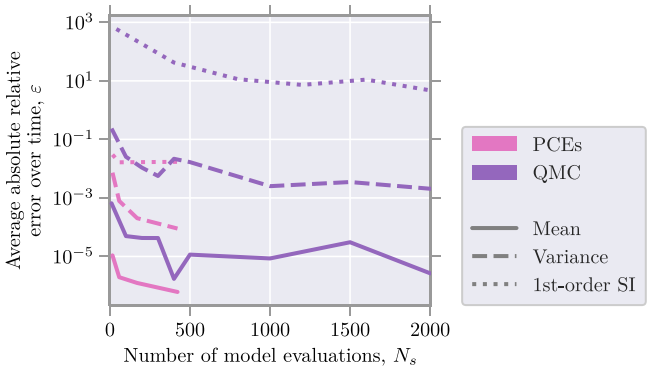

Fig. 2. The error of the mean, variance, and first-order SI while using either the QMC method or PCEs for the UQ and SA of the PEMEC polarization behavior at 80 °C. A 0D semi-empirical model is used as the black box model.

experimental data. Both expressions for ξ were implemented in the 1D in-house solver for PEMEC and compared with each other. Fig. 3 shows the resulting polarization curves and water content distribution inside the MEA.

As we realize from Fig. 3(a), the variation of the definition of the EOD coefficient leads to different shapes of the polarization curve. With a closer look at the polarization curves, both approaches lead to a nearly identical curve for low current densities up to $1\,\mathrm{A\,cm^{-2}}$. For higher current densities, the cell voltage increases non-linear with the use of the definition of Springer et al. [46], while the cell voltage resulting from the definition of Zawodzinski et al. [47] increases linearly with increasing current densities. In addition to that, the distribution of electronic and protonic potentials also varies, especially on the anode side (see Fig. 3(b)).

In Fig. 3(c), the water-content distribution through the MEA resulting from the 1D model while using the different definitions of the EOD coefficient shows a qualitatively similar shape. However, with the use of the definition formulated by Springer et al. [46], the values of water content vary more widely with a decreasing water content through the aCL and the membrane and a sharp increase towards the cCL. Using the EOD coefficient according to Zawodzinski et al. [47], the water content results in a more constant shape. Of course, the observed variation in the water-content distribution affects the profile of effective protonic conductivity since it is a function of λ (see Fig. 3(d)). The discontinuities in its distribution between the PEM and CLs are due to the lower ionomer volume fraction in the CLs (see Table 6).

Lastly, we provide the supporting Fig. A.5, showing the through-plane potential profiles, water-content distribution, and σ_p^{eff}-distribution at different current densities. We again draw readers' attention to the fact that electronic and protonic potentials, and the water content are coupled. This can be realized by taking a careful look at the Eqs. (2), (3), (4), and (8). The EOD term in strongly depends on the flux of protons j_p, whereas the proton conductivity is a function of water content, λ. Furthermore, the electronic and protonic potentials are mutually related via the reactions in CLs. The supporting Fig. A.5 underscores how the two different models for the EOD coefficient leads to varying water-content distribution, especially at high current densities. Therefore, the profile of proton conductivity and the protonic and electronic potentials are strongly influenced, resulting in the deviations of the polarization curves discussed earlier.

Reference exchange current density and volume-specific surface area of the catalyst layer Similar to the EOD coefficient, values for the reference exchange current density $i_{0,a/c}^{\mathrm{ref}}$ and the activation energy $E_{\mathrm{A},a/c}$ must also be chosen from literature or based on experiments. Carmo et al. [60] reported their values for $T_{\mathrm{ref}} = 80\,^{\circ}\mathrm{C}$:

Table 8
Literature data for the product, $a_{a/c}^{\mathrm{cat}} \cdot i_{0,a/c}$, at $T = 80\,^{\circ}\mathrm{C}$.

Case	Reference	$a_a^{\mathrm{cat}} \cdot i_{0,a}$ $[\mathrm{A\,cm^{-3}}]$	$a_c^{\mathrm{cat}} \cdot i_{0,c}$ $[\mathrm{A\,cm^{-3}}]$
1	[10]	$5 \cdot 10^{-3}$	50
2	[10]	0.02	200
3	[10]	0.04	400
4	[27]	0.066	24 495.68

- Pt-Ir anode: $i_{0,a}^{\mathrm{ref}} \approx 1 \cdot 10^{-7}\,\mathrm{A\,cm^{-2}}$ with a large variability
- Pt cathode: $i_{0,c}^{\mathrm{ref}} \approx 1 \cdot 10^{-3}\,\mathrm{A\,cm^{-2}}$

The chosen values for $i_{0,a/c}^{\mathrm{ref}}$ by García-Salaberri [10] and Trinke [27] refer to the model of García-Valverde et al. [30], whose values are close to the ones reported by Carmo et al. [60]. The CL-specific surface area also exhibits high variability in its values in the literature. For instance, García-Salaberri [10] and Chen et al. [33] consider its dependency on the liquid water saturation. Other papers specify values for the product of the exchange current density with the specific surface area. Moreover, Goshtasbi et al. [16] pointed out that the exchange current density with the specific surface area always appears as a product in the Butler–Volmer Eq. (10), which makes these two parameters non-identifiable. Pant et al. [17] also indicated the same. Therefore, we considered their uncertainty as a product in the model. In future work, we could apply the Rosenblatt transformation [61] to decorrelate the parameters before applying SA.

In Table 8, we present the calculated values of the product, $a_{a/c}^{\mathrm{cat}} \cdot i_{0,a/c}$, at $T = 80\,^{\circ}\mathrm{C}$ without considering $a_{a/c}^{\mathrm{cat}}$-dependence on the liquid water saturation. We also realize the wide range in their resulting values, whose impact on the polarization behavior of PEMECs is depicted in Fig. 4. For the computations in Fig. 4, the EOD coefficient in Eq. (23) is used.

The resulting polarization curves highly differ from each other. Case 1 from García-Salaberri [10] shows an increased cell voltage for the whole range of considered current densities of nearly 0.1 V. Here, the polarization curve is quantitatively affected by the different cases in Table 8, but not qualitatively.

5.2 Validation against experimental data

To validate the 1D PEMEC model, the experimental data of Chandesris et al. [43] are consulted. For the comparison between the computed polarization behavior and the experimental one, we use the parameter setup in Table 6, but we adjust the layer thicknesses for aPTL and cPTL, as reported by Chandesris et al. [43] and García-Salaberri [10]. For example, $l_{\mathrm{aPTL}} = 1.4\,\mathrm{mm}$, and $l_{\mathrm{cPTL}} = 0.235\,\mathrm{mm}$. In addition, we have to adopt the values for the product of $a_{a/c}^{\mathrm{cat}} \cdot i_{0,a/c}^{\mathrm{ref}}$. In the previous section, we commented on the variability in its values. Therefore, we use two different approaches for our validation to tackle issues related to its variability and uncertainty.

5.2.1 Deterministic approach

We first simulate the polarization behavior of a PEMEC, using constant (i.e., non-random) values for the product of $a_{a/c}^{\mathrm{cat}} \cdot i_{0,a/c}^{\mathrm{ref}}$. Its value for the anode is equal to $0.021\,\mathrm{A\,cm^{-3}}$, whereas for the cathode is equal to $210\,\mathrm{A\,cm^{-3}}$. These values were reported by García-Salaberri [10] and most probably computed based on least-squares fitting.

In Fig. 5, we observe that the computed polarization curve is in good agreement with the experimental data for $T = 80\,^{\circ}\mathrm{C}$ and $T = 60\,^{\circ}\mathrm{C}$. However, a deviation is noted for $T = 40\,^{\circ}\mathrm{C}$. This discrepancy can be associated with the simplifying assumptions in the mathematical model (e.g., isothermal conditions, constant RH and s). Furthermore, insufficient measurement data to adequately infer, learn, and calibrate the constitutive relations, which hold for different model parameters, can also cause this deviation.

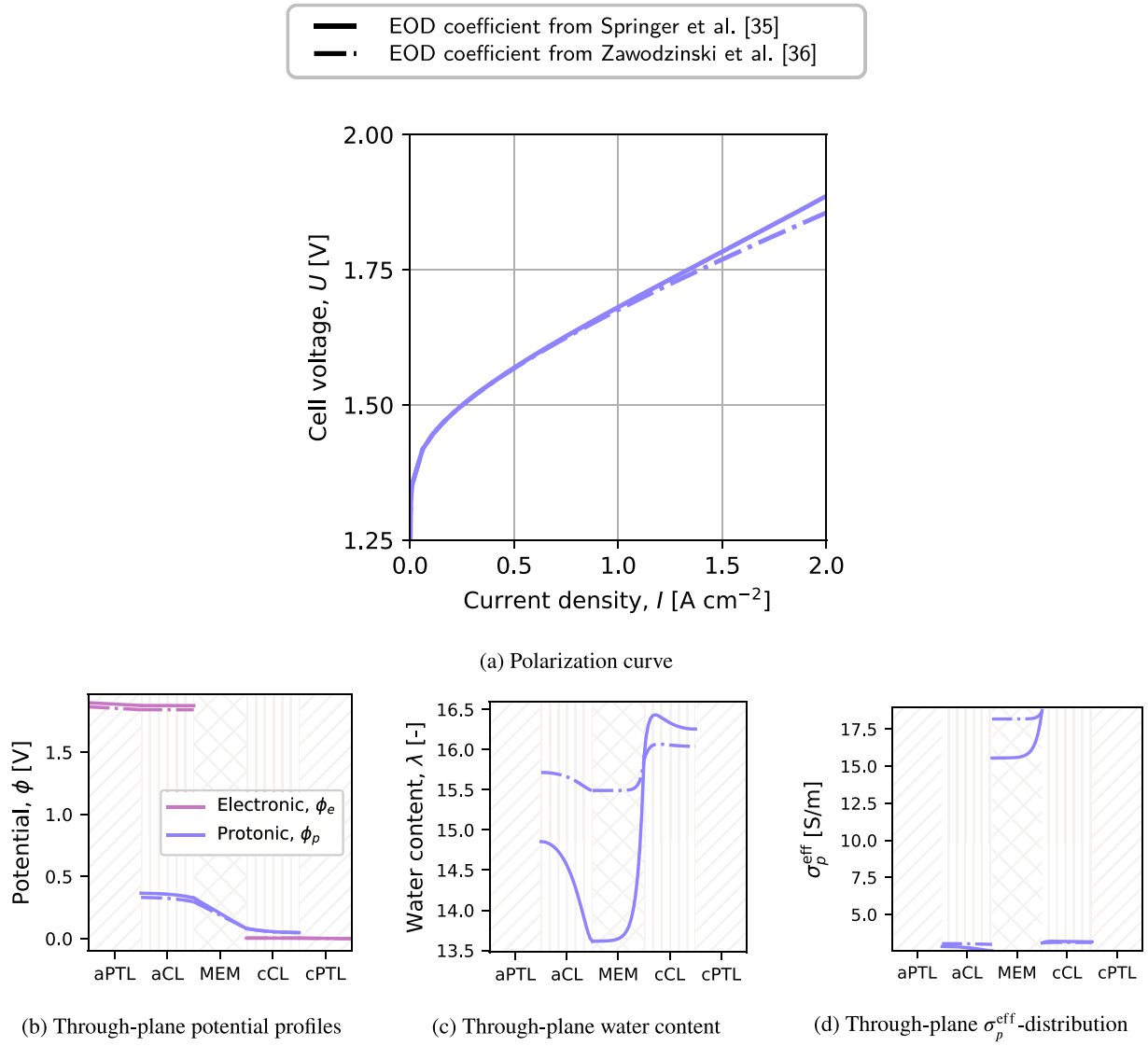

(a) Polarization curve

(b) Through-plane potential profiles

(c) Through-plane water content

(d) Through-plane σ_p^{eff}-distribution

Fig. 3. Comparison of the polarization curve and the through-plane potential profiles, water-content distribution, and σ_p^{eff}-distribution at $I = 2.0\,\text{A cm}^{-2}$ resulting from the different EOD-coefficient models, as proposed by Springer et al. [46] vs. Zawodzinski et al. [47].

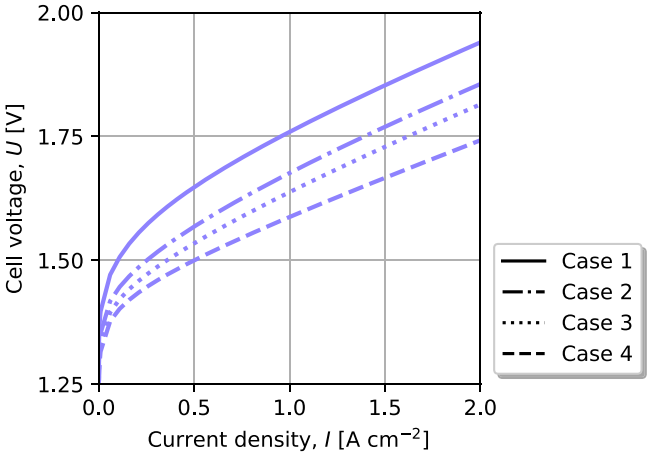

Fig. 4. Comparison of the polarization curve resulting from different values of the product, $a_{a/c}^{\text{cat}} \cdot i_{0,a/c}$ (see Table 8).

Table 9
Uncertainty range and probability distribution functions (PDF) of the $a_{a/c}^{\text{cat}} \cdot i_{0,a/c}^{\text{ref}}$ values for the stochastic modeling. Here, $\mathcal{U}(\cdot,\cdot)$ indicates the uniform probability distribution.

Parameter	Unit	Uncertainty range	Distribution
$a_a^{\text{cat}} \cdot i_{0,a}^{\text{ref}}$	A cm^{-3}	[0.005, 0.04]	$\mathcal{U}(0.005, 0.04)$
$a_c^{\text{cat}} \cdot i_{0,c}^{\text{ref}}$	A cm^{-3}	[50, 400]	$\mathcal{U}(50, 400)$

5.2.2 Stochastic approach

To account for uncertainty and variability of the $a_{a/c}^{\text{cat}} \cdot i_{0,a/c}^{\text{ref}}$ values, we model it as stochastic (random) variables and assign to it a uniform probability distribution function (PDF), as shown in Table 9. Fig. 6 compares the polarization behavior computed from the 1D PEMEC model, described earlier, with the corresponding experimental data from Chandesris et al. [43]. In this figure, the blue shaded area shows the PI of our model prediction. The experimental observations are represented in magenta color and lie within the 90% prediction interval, even in the case of $T = 40\,°\text{C}$.

5.3 Sensitivity analyses

Finally, the SA result for the 1D PEMEC model, when accounting for uncertainty and variability of the $a_{a/c}^{\text{cat}} \cdot i_{0,a/c}^{\text{ref}}$ values (two in total

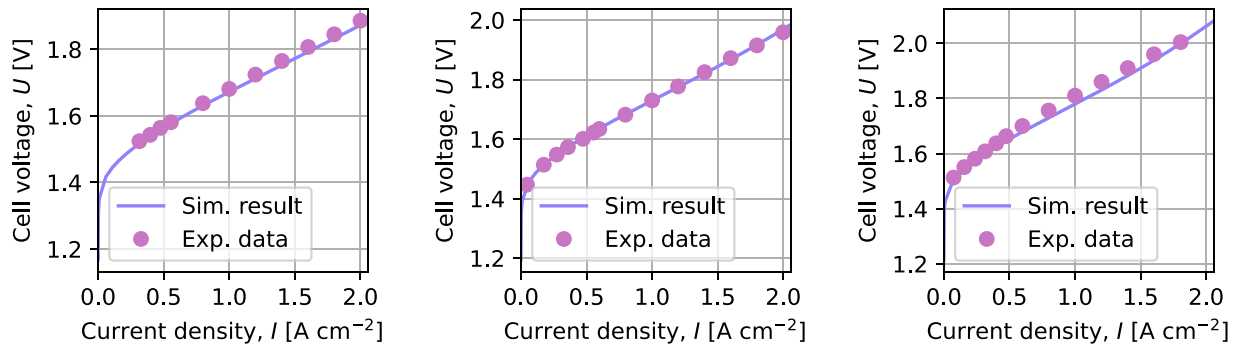

(a) $T = 80\,°C,\ RH = 0.9,\ s = 0.5$ (b) $T = 60\,°C,\ RH = 0.95,\ s = 0.5$ (c) $T = 40\,°C,\ RH = 1.0,\ s = 0.70$

Fig. 5. Validation against experimental data from Chandesris et al. [43] by means of deterministic modeling.

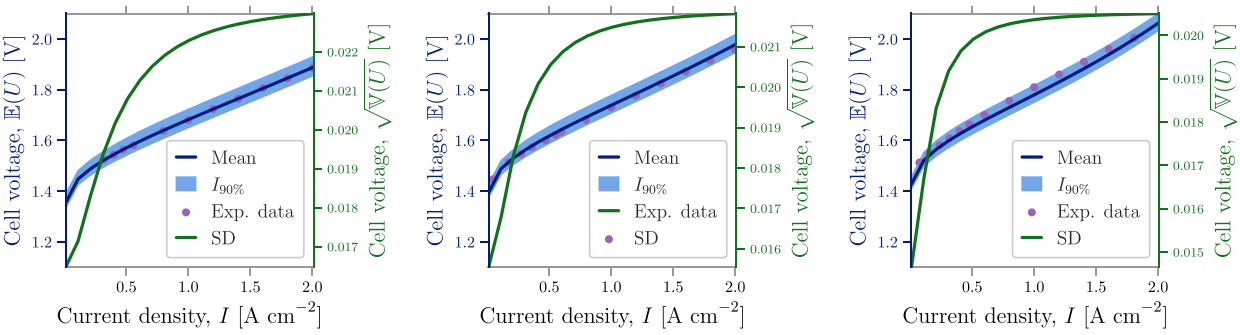

(a) $T = 80\,°C,\ RH = 0.9,\ s = 0.5$ (b) $T = 60\,°C,\ RH = 0.95,\ s = 0.5$ (c) $T = 40\,°C,\ RH = 1.0,\ s = 0.70$

Fig. 6. Validation against experimental data from Chandesris et al. [43] by means of stochastic modeling.

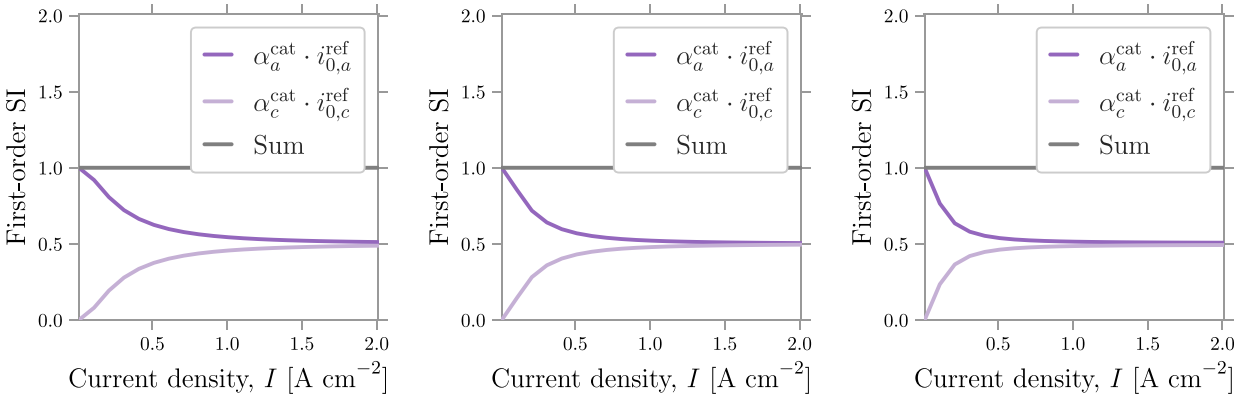

(a) $T = 80\,°C,\ RH = 0.9,\ s = 0.5$ (b) $T = 60\,°C,\ RH = 0.95,\ s = 0.5$ (c) $T = 40\,°C,\ RH = 1.0,\ s = 0.70$

Fig. 7. First-order SI for the uncertain product, $a_{a/c}^{\text{cat}} \cdot i_{0,a/c}^{\text{ref}}$.

parameters for this SA scenario, Table 9), is shown in Fig. 7. SI are employed as a sensitivity measure of the modeling outcome on the individual input parameters. Since we did not observe a significant difference between first-order and total SI, meaning that these two input parameters do not significantly interact with each other, we only plot the first-order indices in Fig. 7. We observe that the $a_a^{\text{cat}} \cdot i_{0,a}^{\text{ref}}$ plays a crucial role when the current density is lower than $0.5\,\text{A/cm}^2$. Thus, the reaction kinetics of OER seem to be highly influential at low current densities compared to HER. Furthermore, different operating conditions also impact the sensitivity of the computed polarization behavior.

We are conducting another SA study (Figs. 8 and A.6) to understand better the interplay between different layer thicknesses and the polarization behavior of PEMECs. We assume that the layer thicknesses behave as random variables, are independent of each other, and assign them a uniform PDF as presented in Table 10. In Fig. 8, we present the first-order SI. Therefore, we can explain which layer is responsible for deviations from the mean polarization curve in the range of investigated current densities. The PEM thickness influences the polarization behavior for higher current densities than $1.0\,\text{A/cm}^2$.

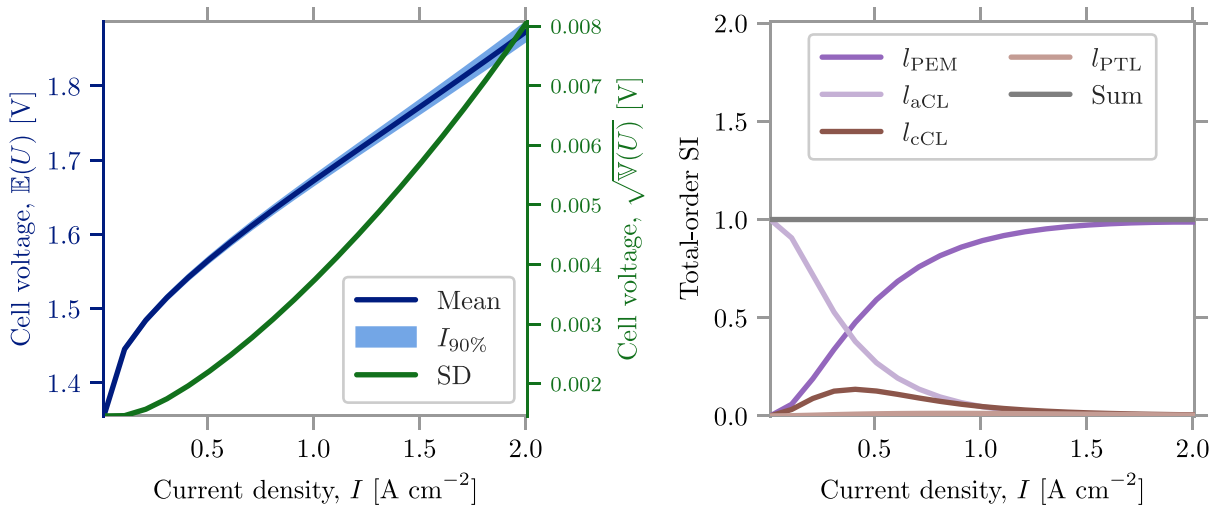

(a) Cell potential

(b) First-order SI

Fig. 8. UQ and SA of the polarization behavior at 80 °C for $i_{0,a}^{\mathrm{ref}} = 10^{-7}$ A cm^{-2} and $i_{0,c}^{\mathrm{ref}} = 10^{-3}$ A cm^{-2} by means of the 1D PEMEC model, while assuming the layer thicknesses as random variables.

Table 10
Uncertainty range and probability distribution functions (PDF) of the layer thicknesses, taken into account for the global SA.

Parameter	Unit	Uncertainty range	Distribution
MEM thickness, l_{PEM}	μm	[170, 190]	$\mathcal{U}(170, 190)$
aCL thickness, l_{aCL}	μm	[11, 13]	$\mathcal{U}(11, 13)$
cCL thickness, l_{cCL}	μm	[11, 13]	$\mathcal{U}(11, 13)$
PTLs thickness, l_{PTL}	μm	[150, 250]	$\mathcal{U}(150, 250)$

On the contrary, the PTL thicknesses do not show any effects within the entire current-density range. Electron conduction within the PTLs and CLs does not influence much the cell voltage because of the high values of the effective electronic conductivity within these layers (Table 6). The electronic potential linearly drops within PTLs, but the decrease is really small compared to the ones in CLs and PEM.

Regarding the CL thicknesses, the SA in Fig. 8 shows that the anode catalyst layer is more crucial than the cathode one, in the regime of low current densities. This is mainly due to the difference of the reference exchange current density in the aCL and cCL. Carmo et al. [60] reported four orders of magnitude difference, which is used in our simulations and for the SA in Fig. 8. For example, when we decrease the reference exchange current density of cCL (supporting Fig. A.6), then both CLs exhibit similar reaction kinetics. As a consequence, their layer thicknesses influence almost the same the polarization behavior. However, we observe that the cell voltage increases (supporting Fig. A.6(a)) compared to the initial configuration (Fig. 8(a)).

Our 1D macroscopic model might be expanded with a 1D microscopic model for CLs, as already reported for PEMFCs [32,62,63]. This 1D microscopic model, then, would offer to explore the effects of CLs structure, and especially its loading, volume-specific surface area, and thickness, on PEMEC performance. Thankfully, the computational model and framework presented in this work can be easily expanded upon and serve as a starting point for further investigation.

6 Conclusions

In this work, we presented a one-dimensional mathematical model that describes six transport phenomena taking place in a five-layer PEMEC. We implemented this model in Python and demonstrated how it can be evaluated numerically with the help of the solve_bvp solver from the submodule scipy.integrate. The computational model robustness led to a reduced simulation time of a few minutes, which was an asset for our UQ and SA purposes. A framework for UQ and global SA based on the libraries Chaospy [25] and Uncertainpy [26] was implemented and used to study the prediction capabilities and accuracy of the 1D model. The QMC method and PCEs were two methods available in this framework. As already reported by Tennøe et al. [26], PCEs proved to be more efficient in our test cases as well, where the parameter space was small enough.

We have demonstrated how PEMECs benefit from UQ and SA. Understanding the interplay between input parameters and model output contributes to improving model adequacy and measurement accuracy for parameter estimation and, ultimately, to the PEMEC optimization and better design. To a similar conclusion, Xie et al. [64] has also pointed out that global SA provides valuable information for analysis and design in the field of chemical engineering, in general. In the SA studies, we observed that the anode kinetics have higher impact on the polarization behavior than the cathode kinetics. Furthermore, the membrane thickness, closely related to ohmic losses, is another critical parameter. Moreover, many of the input parameters, e.g., the exchange current density, the CL volume-specific surface area, the EOD coefficient, highly vary in literature. Thus, appropriate experiments for their precise measurement are required and will contribute to the improvement of the model accuracy. In future work, we should perform an exhaustive analysis by investigating the influence of every input parameter on the polarization behavior and assigning realistic uncertainty distribution to them. In the former sensitivity analyses, we used uniform distributions, but distributions, estimated on experimental data, would have been preferred.

CRediT authorship contribution statement

Violeta Karyofylli: Writing – original draft, Visualization, Validation, Software, Methodology, Investigation, Conceptualization. **Yannik Danner:** Writing – original draft, Visualization, Validation, Software, Methodology, Investigation. **K. Ashoke Raman:** Writing – review & editing, Investigation. **Hans Kungl:** Writing – review & editing, Supervision, Project administration, Funding acquisition. **André Karl:** Writing – review & editing, Project administration. **Eva Jodat:** Writing – review & editing, Project administration. **Rüdiger-A. Eichel:** Writing – review & editing, Supervision, Project administration, Funding acquisition.

Declaration of competing interest

The authors declare that they have no known competing financial interests or personal relationships that could have appeared to influence the work reported in this paper.

Data availability

Data will be made available on request.

Acknowledgment

The authors gratefully acknowledge the financial support by the German Federal Ministry of Education and Research (BMBF) within the H2Giga project DERIEL (grant number 03HY122C). The authors would also like to thank Sebastian B. C. Lehmann for his contribution to the graphical designs.

Appendix. Supporting material

A.1. Definition of ARE

In Section 4.1, we used the absolute relative error averaged over current density to compare QMC against PCEs:

$$\varepsilon = \frac{1}{I}\int \frac{\Psi_{exact} - \Psi}{\Psi_{exact}} di \tag{38}$$

with Ψ representing in general either the mean, variance, or first-order SI. Since an exact solution is not known for this problem, we employ the QMC method with $N_s = 200000$ to calculate Ψ_{exact}. The Ψ without subscript is computed via either the QMC method or PCEs. The total range of current densities is represented by I.

Acronyms

Notation	Description
aCH	anodic channel
aCL	anodic catalyst layer
AEL	alkaline electrolysis
aPTL	anodic porous transport layer
ARE	absolute relative error
BC	boundary condition
BoP	balance of plant
BVP	boundary value problem
CAPEX	capital expenditure
cCH	cathodic channel
cCL	cathodic catalyst layer
CL	catalyst layer
cPTL	cathodic porous transport layer
EC	electrolytic cell
EOD	electro-osmotic drag
GUI	graphical user interface
HER	hydrogen evolution reaction
MATLAB	matrix laboratory
MC	Monte Carlo
MEA	membrane-electrode assembly
MEM	membrane
ODE	ordinary differential equation
OER	oxygen evolution reaction
OpenFOAM	open source field operation and manipulation
PCE	polynomial chaos expansion
PEM	proton-exchange membrane
PEMEC	PEM electrolytic cell
PEMEL	PEM electrolysis
PEMFC	PEM fuel cell
PI	prediction interval
Pt	platinum
PTLs	porous transport layers
PYPL	PopularitY of Programming Language
QMC	quasi-Monte Carlo
QoIs	quantities of interest
SA	sensitivity analysis
SD	standard deviation
SI	Sobol indices
UQ	uncertainty quantification
VB	variational Bayes

List of Symbols

Sign	Description	Unit
D_λ	water diffusivity in the ionomer phase	$m^2\ s^{-1}$
$D^{\text{ref}}_{H_2O,a/c}$	reference diffusivity of water vapor	$m^2\ s^{-1}$
EW_m	equivalent weight of dry membrane	$kg\ mol^{-1}$
EW_w	equivalent weight of water	$kg\ mol^{-1}$
$E_{A,a/c}$	activation energy	$J\ mol^{-1}$
E_λ	diffusion activation energy	$J\ mol^{-1}$
E_σ	activation energy of proton conduction	$J\ mol^{-1}$
$E^{\text{rev}}_{a/c}$	reversible voltage of the OER or HER	V
$E_{a/d}$	sorption/desorption activation energy	$J\ mol^{-1}$
F	Faraday constant	$C\ mol^{-1}$
I_χ	prediction interval	–
I_j	interfaces between the domain intervals	–
N_s	number of model evaluations	–
P^{ref}_g	reference pressure	Pa
$P^{\text{sat}}_{H_2O}$	saturation pressure of water vapor	Pa
$P_{g,a/c}$	operating pressure at the anode or cathode	Pa
R_{sep}	separator resistance	$\Omega\ cm^2$
$R_{a/c}$	anodic or cathodic reaction rates	$A\ m^{-3}$
R_e	electrode resistance	$\Omega\ cm^2$
R	gas constant	$J\ K^{-1}\ mol^{-1}$
S_i	first-order Sobol sensitivity index	–
T^{ref}	reference temperature	K
T	operating temperature	K
U_N	Nernst voltage	V
U_Ω	ohmic drop due to electron and ion conduction	V
U_{kin}	kinetic overpotential	V
$V_{m/w}$	molar volume of dry electrolyte per SO_3^- group or liquid water	$m^3\ mol^{-1}$
Y_{H_2}	partial pressure increase factors for hydrogen (cathode)	$bar\ cm^2\ A^{-1}$
Y_{O_2}	partial pressure increase factors for oxygen (anode)	$bar\ cm^2\ A^{-1}$
$\Delta H_{a/c}$	enthalpy change of OER (anode) or HER (cathode)	$J\ mol^{-1}$
$\Delta S_{a/c}$	entropy change of OER (anode) or HER (cathode)	$J\ mol^{-1}\ K^{-1}$
Ω_i	domain interval, corresponding to a layer	–

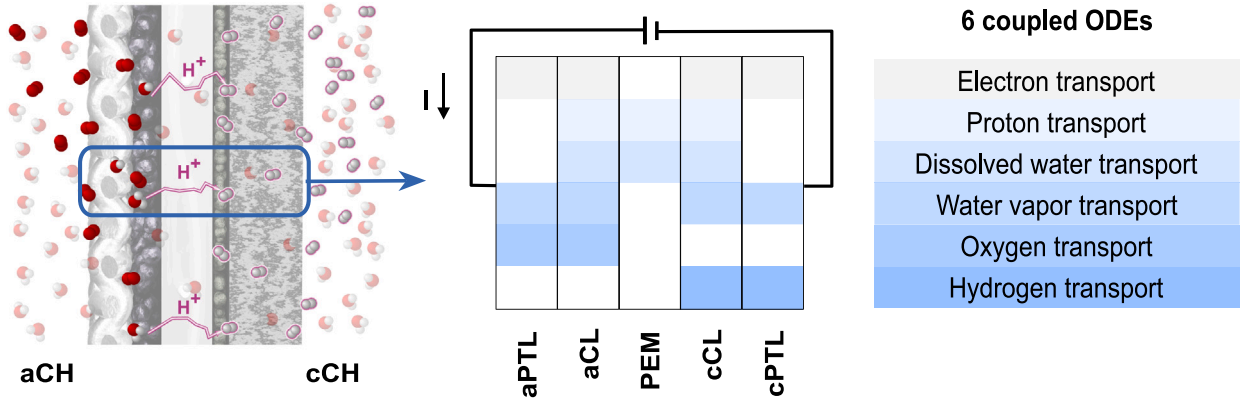

Fig. A.1. Schematic overview of five layers within PEMECs: Computational domain and equations included in the model.

Sign	Description	Unit
Ω	computational domain	–
α	Tafel slope	V
χ	the $(100 \cdot \chi)$th percentile	–
$\eta_{a/c}$	anodic or cathodic activation overpotential	V
λ_{eq}	equilibrium water content in ionomer	–
λ	water content in ionomer phase	–
$\mathbb{E}$	mean (expectation) value	–
$\mathbb{V}$	variance	–
RH	relative humidity	–
ϕ_e	electronic potential	V
ϕ_p	protonic potential	V
ρ_m	density of dry membrane	kg m^{-3}
ρ_w	density of water	kg m^{-3}
σ_e^{eff}	effective electron conductivity	S m^{-1}
σ_p^{eff}	effective proton conductivity	S m^{-1}
τ_p	pore tortuosity	–
$\epsilon_{a/c}^{\text{cat}}$	catalyst volume fraction	–
ϵ_m	ionomer volume fraction	–
ϵ_p	pore volume fraction	–
ξ	EOD coefficient	–
$a_{a/c}^{\text{cat}}$	volume-specific surface area of anode or cathode catalyst layer	m^{-1}
$a_{a/c}$	charge transfer coefficient	–
$d_{a/c}^{\text{cat}}$	catalyst particle diameter at the anode or cathode	m
f_v	water volume fraction in the ionomer phase	–
i_0	exchange current density	A m^{-2}
$i_{0,a/c}^{\text{ref}}$	anodic or cathodic reference exchange current density	A m^{-2}
$i_{0,a/c}$	anodic or cathodic exchange current density	A m^{-2}
k_a^{ref}	reference sorption coefficient	m s^{-1}
k_d^{ref}	reference desorption coefficient	m s^{-1}
$k_{a/d}$	sorption/desorption mass-transfer coefficient	m s^{-1}
l_{Ω_i}	layer thickness	m
n_s	coverage factor	–
s	liquid water saturation	–
x_k	molar fraction of the kth gas species	–

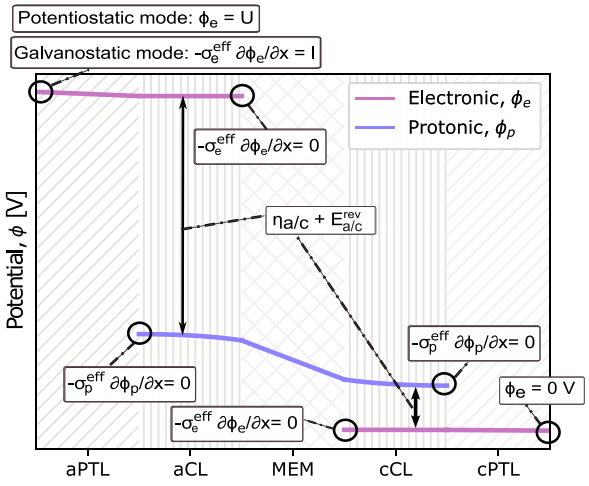

Fig. A.2. Schematic overview of local electron- and proton-potential distribution within the computational domain.

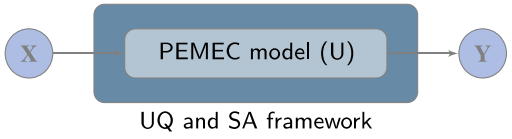

Fig. A.3. Black box model for UQ and SA in PEMEC.

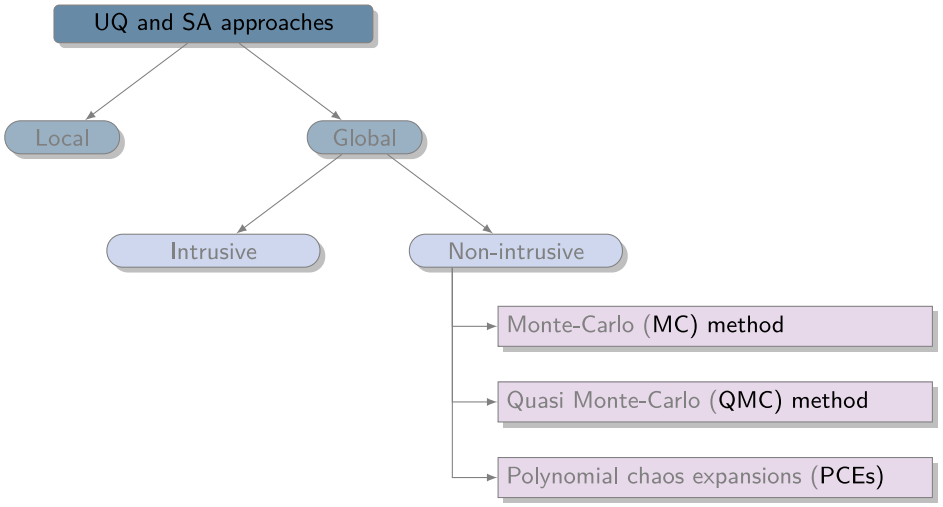

Fig. A.4. Classification of methods for UQ and SA.

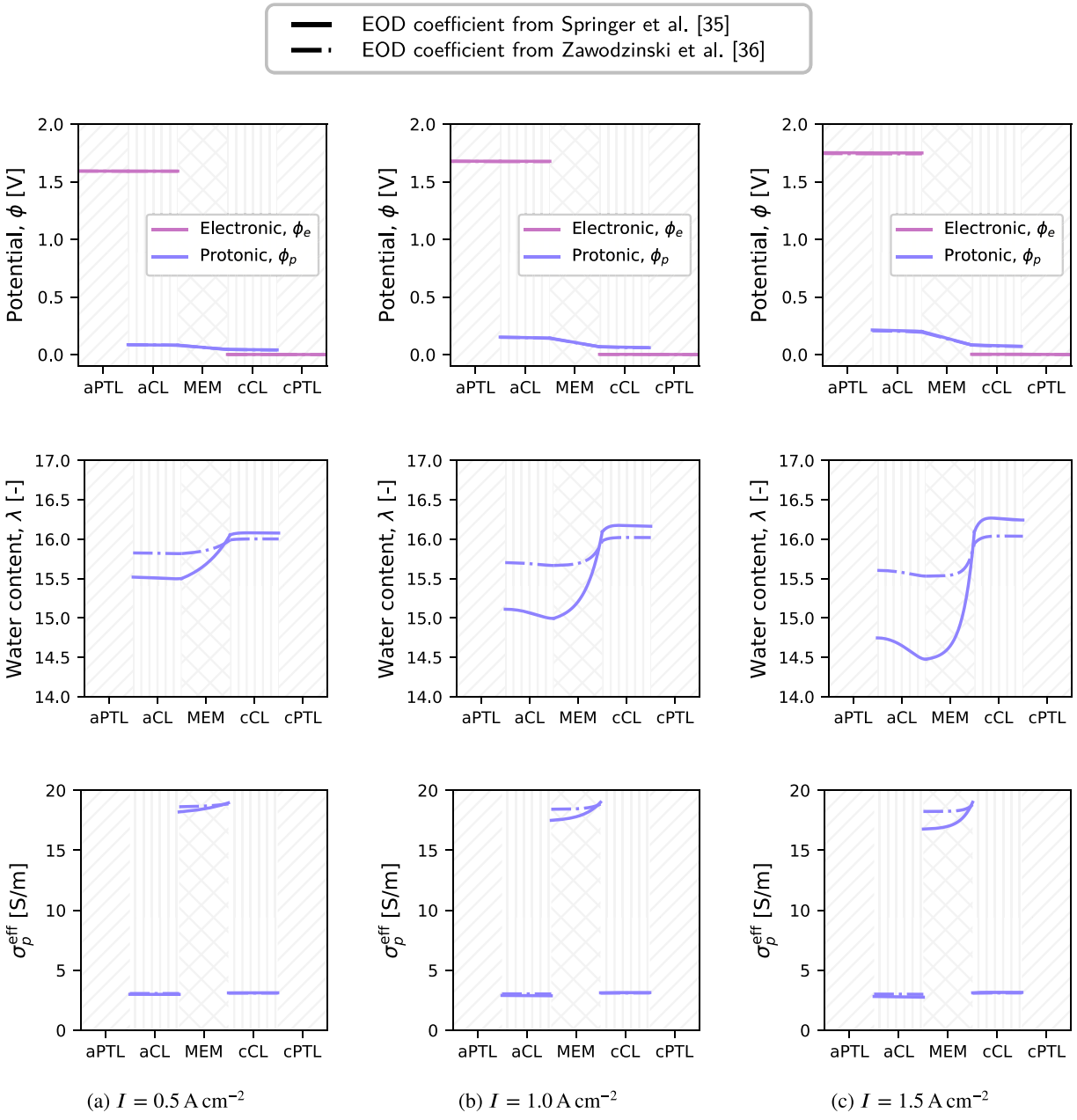

Fig. A.5. Comparison of the through-plane potential profiles, water-content distribution, and σ_p^{eff}-distribution, resulting from the different EOD-coefficient models, as proposed by Springer et al. [46] vs. Zawodzinski et al. [47], at different current densities.

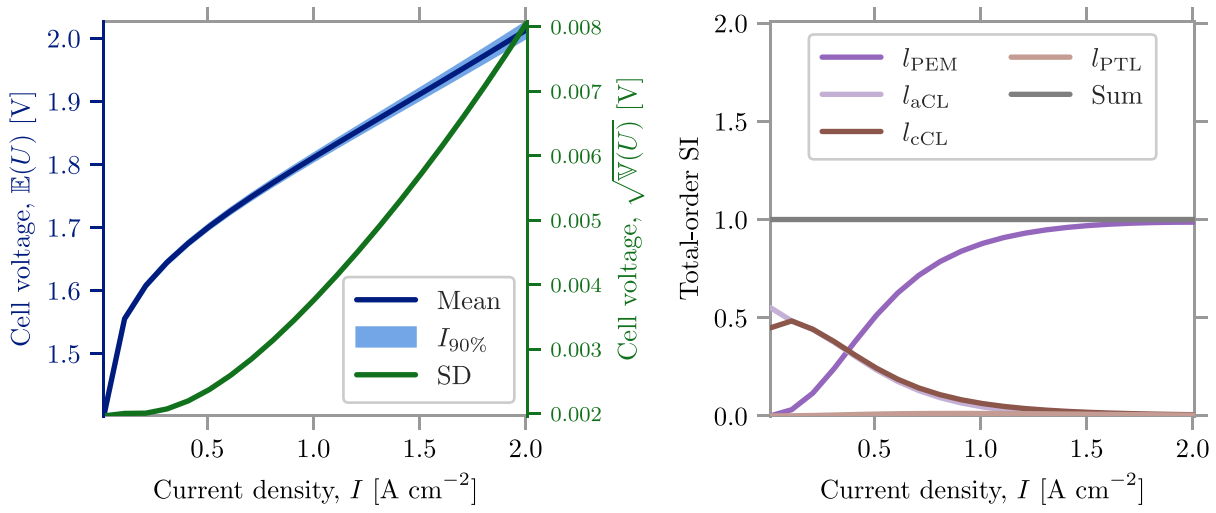

(a) Cell potential

(b) First-order SI

Fig. A.6. UQ and SA of the polarization behavior at 80 °C for $i_{0,a}^{\mathrm{ref}} = 10^{-7}$ A cm^{-2} and $i_{0,c}^{\mathrm{ref}} = 10^{-5}$ A cm^{-2} by means of the 1D PEMEC model, while assuming the layer thicknesses as random variables.

A.2. Supporting figures

See Figs. A.1–A.6.

References

[1] M. Holst, S. Aschbrenner, T. Smolinka, C. Voglstätter, G. Grimm, Cost Forecast for Low Temperature Electrolysis-Technology Driven Bottom-Up Prognosis for PEM and Alkaline Water Electrolysis Systems, Fraunhofer ISE, 2021.

[2] Z. Ma, L. Witteman, J.A. Wrubel, G. Bender, A comprehensive modeling method for proton exchange membrane electrolyzer development, Int. J. Hydrogen Energy 46 (34) (2021) 17627–17643.

[3] A. Abdol Rahim, A.S. Tijani, S. Kamarudin, S. Hanapi, An overview of polymer electrolyte membrane electrolyzer for hydrogen production: Modeling and mass transport, J. Power Sources 309 (2016) 56–65.

[4] M. Secanell, A. Putz, P. Wardlaw, V. Zingan, M. Bhaiya, M. Moore, J. Zhou, C. Balen, K. Domican, OpenFCST: An open-source mathematical modelling software for polymer electrolyte fuel cells, ECS Trans. 64 (3) (2014) 655.

[5] S. Haghighi, K. Askari, S. Hamidi, M.M. Rahimi, OPEM: Open source PEM cell simulation tool, J. Open Source Softw. 3 (27) (2018) 676.

[6] J. Gostick, M. Aghighi, J. Hinebaugh, T. Tranter, M.A. Hoeh, H. Day, B. Spellacy, M.H. Sharqawy, A. Bazylak, A. Burns, W. Lehnert, A. Putz, OpenPNM: A pore network modeling package, Comput. Sci. Eng. 18 (4) (2016) 60–74.

[7] D.B.P. Harvey, Development of a Stochastically-Driven, Forward Predictive Performance Model for PEMFCs (Ph.D. thesis), Queen's University, Canada, 2017.

[8] J.-P. Kone, X. Zhang, Y. Yan, S. Adegbite, An open-source toolbox for PEM fuel cell simulation, Computation 6 (2) (2018).

[9] R. Vetter, J.O. Schumacher, Free open reference implementation of a two-phase PEM fuel cell model, Comput. Phys. Comm. 234 (2019) 223–234.

[10] P.A. García-Salaberri, 1D two-phase, non-isothermal modeling of a proton exchange membrane water electrolyzer: An optimization perspective, J. Power Sources 521 (2022) 230915.

[11] C.R. Randall, c-randall/p2d_pemfc_2phase: v1.0, Zenodo, 2022, http://dx.doi.org/10.5281/zenodo.5823445.

[12] N. Weber, L. Knüpfer, S.B. Beale, W. Lehnert, U. Reimer, S. Zhang, P. Ferreira-Aparicio, A. M. Chaparro, Open-source computational model for polymer electrolyte fuel cells, OpenFOAM® J. 3 (2023) 26–48.

[13] S. Zhang, S. Hess, H. Marschall, U. Reimer, S. Beale, W. Lehnert, openFuelCell2: A new computational tool for fuel cells, electrolyzers, and other electrochemical devices and processes, Comput. Phys. Commun. 298 (2024) 109092.

[14] R. Vetter, J.O. Schumacher, Experimental parameter uncertainty in proton exchange membrane fuel cell modeling. Part I: Scatter in material parameterization, J. Power Sources 438 (2019) 227018.

[15] R. Vetter, J.O. Schumacher, Experimental parameter uncertainty in proton exchange membrane fuel cell modeling. Part II: Sensitivity analysis and importance ranking, J. Power Sources 439 (2019) 126529.

[16] A. Goshtasbi, J. Chen, J.R. Waldecker, S. Hirano, T. Ersal, Effective parameterization of PEM fuel cell models—Part I: Sensitivity analysis and parameter identifiability, J. Electrochem. Soc. 167 (4) (2020).

[17] L.M. Pant, S. Stewart, N. Craig, A.Z. Weber, Critical parameter identification of fuel-cell models using sensitivity analysis, J. Electrochem. Soc. 168 (7) (2021).

[18] B. Laoun, M.W. Naceur, A. Khellaf, A.M. Kannan, Global sensitivity analysis of proton exchange membrane fuel cell model, Int. J. Hydrogen Energy 41 (22) (2016) 9521–9528.

[19] L. Xu, C. Fang, J. Hu, S. Cheng, J. Li, M. Ouyang, W. Lehnert, Parameter extraction and uncertainty analysis of a proton exchange membrane fuel cell system based on Monte Carlo simulation, Int. J. Hydrogen Energy 42 (4) (2017) 2309–2326.

[20] X. Liu, Y. Yang, L. Zhang, S. Zhou, L. Xu, C. Xie, B. Zhao, L. Zhang, Uncertainty assessment of a semi-empirical output voltage model for proton exchange membrane fuel cells, Int. J. Hydrogen Energy 48 (29) (2023) 11071–11085.

[21] D.M. Zhou, T.T. Nguyen, E. Breaz, D.D. Zhao, S. Clenet, F. Gao, Global parameters sensitivity analysis and development of a two-dimensional real-time model of proton-exchange-membrane fuel cells, Energy Convers. Manage. (ISSN: 0196-8904) 162 (2018) 276–292.

[22] I. Sobol', Global sensitivity indices for nonlinear mathematical models and their Monte Carlo estimates, Math. Comput. Simulation 55 (1) (2001) 271–280.

[23] V. Kannan, H.S. Xue, K.A. Raman, J.S. Chen, A. Fisher, E. Birgersson, Quantifying operating uncertainties of a PEMFC - Monte Carlo-machine learning based approach, Renew. Energy 158 (2020) 343–359.

[24] M. Pan, C. Pan, J. Liao, C. Li, R. Huang, Q. Wang, Assessment of sensitivity to evaluate the impact of operating parameters on stability and performance in proton exchange membrane fuel cells, Energies 14 (14) (2021).

[25] J. Feinberg, H.P. Langtangen, Chaospy: An open source tool for designing methods of uncertainty quantification, J. Comput. Sci. (ISSN: 1877-7503) 11 (2015) 46–57.

[26] S. Tennøe, G. Halnes, G.T. Einevoll, Uncertainpy: A Python toolbox for uncertainty quantification and sensitivity analysis in computational neuroscience, Front. Neuroinform. 12 (2018).

[27] P. Trinke, Experimental and Model-Based Investigations on Gas Crossover in Polymer Electrolyte Membrane Water Electrolyzers (Ph.D. thesis), Gottfried Wilhelm Leibniz Universität, Hannover, 2021.

[28] A. Goshtasbi, B.L. Pence, J. Chen, M.A. DeBolt, C. Wang, J.R. Waldecker, S. Hirano, T. Ersal, A mathematical model toward real-time monitoring of automotive PEM fuel cells, J. Electrochem. Soc. 167 (2) (2020) 024518.

[29] V. Sulzer, P. Mohtat, J.B. Siegel, Reduced-order modeling of PEM fuel cells using asymptotic analysis, 2022, ECSarXiv.

[30] R. García-Valverde, N. Espinosa, A. Urbina, Simple PEM water electrolyser model and experimental validation, Int. J. Hydrogen Energy 37 (2) (2012) 1927–1938.

[31] D. Falcão, A.M.F.R. Pinto, A review on PEM electrolyzer modelling: Guidelines for beginners, J. Clean. Prod. 261 (2020).

[32] A. Sánchez-Ramos, J.T. Gostick, P.A. García-Salaberri, Modeling the Effect of Low Pt loading Cathode Catalyst Layer in Polymer Electrolyte Fuel Cells: Part I. Model Formulation and Validation, J. Electrochem. Soc. 168 (12) (2021) 124514.

[33] Q. Chen, Y. Wang, F. Yang, H. Xu, Two-dimensional multi-physics modeling of porous transport layer in polymer electrolyte membrane electrolyzer for water splitting, Int. J. Hydrogen Energy 45 (58) (2020) 32984–32994.

[34] N. Urena, M.T. Perez-Prior, B. Levenfeld, P.A. Garcia-Salaberri, On the conductivity of proton-exchange membranes based on multiblock copolymers of sulfonated polysulfone and polyphenylsulfone: An experimental and modeling study, Polymers (Basel) 13 (3) (2021).
[35] P.A. García-Salaberri, D.G. Sánchez, P. Boillat, M. Vera, K.A. Friedrich, Hydration and dehydration cycles in polymer electrolyte fuel cells operated with wet anode and dry cathode feed: A neutron imaging and modeling study, J. Power Sources 359 (2017) 634–655.
[36] G. Inoue, K. Yokoyama, J. Ooyama, T. Terao, T. Tokunaga, N. Kubo, M. Kawase, Theoretical examination of effective oxygen diffusion coefficient and electrical conductivity of polymer electrolyte fuel cell porous components, J. Power Sources 327 (2016) 610–621.
[37] J.C. Cruz, V. Baglio, S. Siracusano, R. Ornelas, L. Ortiz-Frade, L.G. Arriaga, V. Antonucci, A.S. Aricò, Nanosized IrO2 electrocatalysts for oxygen evolution reaction in an spe electrolyzer, J. Nanoparticle Res. 13 (2011) 1639–1646.
[38] F. Hegge, R. Moroni, P. Trinke, B. Bensmann, R. Hanke-Rauschenbach, S. Thiele, S. Vierrath, Three-dimensional microstructure analysis of a polymer electrolyte membrane water electrolyzer anode, J. Power Sources 393 (2018) 62–66.
[39] M. Mandal, M. Moore, M. Secanell, Measurement of the protonic and electronic conductivities of PEM water electrolyzer electrodes, ACS Appl. Mater. Interfaces 12 (44) (2020) 49549–49562.
[40] F. Aubras, J. Deseure, J.J.A. Kadjo, I. Dedigama, J. Majasan, B. Grondin-Perez, J.P. Chabriat, D.J.L. Brett, Two-dimensional model of low-pressure PEM electrolyser: Two-phase flow regime, electrochemical modelling and experimental validation, Int. J. Hydrogen Energy 42 (42) (2017) 26203–26216.
[41] P. Gode, F. Jaouen, G. Lindbergh, A. Lundblad, G. Sundholm, Influence of the composition on the structure and electrochemical characteristics of the PEFC cathode, Electrochim. Acta 48 (28) (2003) 4175–4187.
[42] J. Ramousse, O. Lottin, S. Didierjean, D. Maillet, Heat sources in proton exchange membrane (PEM) fuel cells, J. Power Sources 192 (2) (2009) 435–441.
[43] M. Chandesris, V. Médeau, N. Guillet, S. Chelghoum, D. Thoby, F. Fouda-Onana, Membrane degradation in PEM water electrolyzer: Numerical modeling and experimental evidence of the influence of temperature and current density, Int. J. Hydrogen Energy 40 (3) (2015) 1353–1366.
[44] C.K. Mittelsteadt, J. Staser, Simultaneous water uptake, diffusivity and permeability measurement of perfluorinated sulfonic acid polymer electrolyte membranes, ECS Trans. 41 (1) (2011) 101.
[45] T. Berning, On the nature of electro-osmotic drag, Energies 13 (18) (2020).
[46] T.E. Springer, T.A. Zawodzinski, S. Gottesfeld, Polymer electrolyte fuel cell model, J. Electrochem. Soc. 138 (1991).
[47] T.A. Zawodzinski, J. Davey, J. Valerio, S. Gottesfeld, The water content dependence of electro-osmotic drag in proton-conducting polymer electrolytes, Electrochim. Acta 40 (1995).
[48] T.F. Fuller, J. Newman, Experimental determination of the transport number of water in Nafion 117 membrane, J. Electrochem. Soc. 139 (1992).
[49] S. Zhang, Modeling and Simulation of Polymer Electrolyte Fuel Cells (Ph.D. thesis), 2019.
[50] A. Zinser, G. Papakonstantinou, K. Sundmacher, Analysis of mass transport processes in the anodic porous transport layer in PEM water electrolysers, Int. J. Hydrogen Energy 44 (52) (2019) 28077–28087.
[51] PYPL PopularitY of programming Language, 2023, Worldwide, https://pypl.github.io/PYPL.html.
[52] T. Oden, R. Moser, O. Ghattas, Computer predictions with quantified uncertainty, part I, SIAM News 43 (9) (2010) 1–3.
[53] J.T. Oden, Adaptive multiscale predictive modelling, Acta Numer. 27 (2018) 353–450.
[54] T. Iwanaga, W. Usher, J. Herman, Toward SALib 2.0: Advancing the accessibility and interpretability of global sensitivity analyses, Soc.-Environ. Syst. Model. 4 (2022) 18155.
[55] J. Herman, W. Usher, SALib: An open-source python library for sensitivity analysis, J. Open Source Softw. 2 (9) (2017).
[56] C. Lemieux, Monte Carlo and Quasi-Monte Carlo Sampling, in: Springer series in statistics, Springer, Dordrecht, 2009.
[57] B. Sudret, Global sensitivity analysis using polynomial chaos expansions, Reliab. Eng. Syst. Saf. 93 (7) (2008) 964–979, Bayesian Networks in Dependability.
[58] M. Schalenbach, G. Tjarks, M. Carmo, W. Lueke, M. Mueller, D. Stolten, Acidic or alkaline? Towards a new perspective on the efficiency of water electrolysis, J. Electrochem. Soc. 163 (11) (2016) F3197.
[59] T. Nguyen, D.C. Francom, D. Luscher, J. Wilkerson, Bayesian calibration of a physics-based crystal plasticity and damage model, J. Mech. Phys. Solids 149 (2021) 104284.
[60] M. Carmo, D.L. Fritz, J. Mergel, D. Stolten, A comprehensive review on PEM water electrolysis, Int. J. Hydrogen Energy 38 (12) (2013) 4901–4934.
[61] M. Rosenblatt, Remarks on a multivariate transformation, Ann. Math. Stat. 23 (3) (1952) 470–472.
[62] A. Sánchez-Ramos, J.T. Gostick, P.A. García-Salaberri, Modeling the effect of low Pt loading cathode catalyst layer in polymer electrolyte fuel cells. Part II: Parametric analysis, J. Electrochem. Soc. 169 (7) (2022).
[63] L. Hao, K. Moriyama, W. Gu, C.-Y. Wang, Modeling and experimental validation of Pt loading and electrode composition effects in PEM fuel cells, J. Electrochem. Soc. 162 (8) (2015) F854.
[64] X. Xie, R. Schenkendorf, U. Krewer, Efficient sensitivity analysis and interpretation of parameter correlations in chemical engineering, Reliab. Eng. Syst. Saf. 187 (2019) 159–173.